

1 **3D simulation of an extreme SAID flow channel**

2 **Joaquín Díaz Peña¹, Matthew Zettergren², Joshua Semeter¹, Yukitoshi**
3 **Nishimura¹, Michael Hirsch¹, Brian Walsh³**

4 ¹Department of Electrical Engineering and Center for Space Physics, Boston University, Boston MA

5 ²Department of Physical Sciences, Embry-Riddle Aeronautical University, Daytona Beach FL

6 ³Department of Mechanical Engineering and Center for Space Physics, Boston University, Boston MA

7 **Key Points:**

- 8 • We present a full 4D (3D + time) simulation of an extreme SAID
- 9 • We utilize the GEMINI model for the simulation due to the practicality and eas-
- 10 ness to set arbitrary input files. Though challenges remain.
- 11 • We highlight the importance of inelastic collisions and impact ionization on damp-
- 12 ing the channel velocity, physics not included in GEMINI.

Abstract

Space-based observations of the signatures associated with STEVE show how this phenomenon might be closely related to an extreme version of a SAID channel. Measurements show high velocities ($>4\text{km/s}$), high temperatures ($>4,000\text{ K}$), and very large current density drivers (up to $1\mu\text{A/m}^2$). This phenomena happens in a small range of latitudes, less than a degree, but with a large longitudinal span. In this study, we utilize the GEMINI model to simulate an extreme SAID/STEVE. We assume a FAC density coming from the magnetosphere as the main driver, allowing all other parameters to adjust accordingly. We have two main objectives with this work: show how an extreme SAID can have velocity values comparable or larger than the ones measured under STEVE, and to display the limitations and missing physics that arise due to the extreme values of temperature and velocity. Changes had to be made to GEMINI due to the extreme conditions, particularly some neutral-collision frequencies. The importance of the temperature threshold at which some collision frequencies go outside their respective bounds, as well as significance of the energies that would cause inelastic collisions and impact ionization are displayed and discussed. We illustrate complex structures and behaviors, emphasizing the importance of 3D simulations in capturing these phenomena. Longitudinal structure is emphasized, as the channel develops differently depending on MLT. However, these simulations should be viewed as approximations due to the limited observations available to constrain the model inputs and the assumptions made to achieve sensible results.

1 Introduction

Ionospheric flow channels, characterized by fast, localized plasma flows, significantly influence the dynamics and structure of the ionosphere (Lyons et al., 2016). They affect the distribution of ionospheric plasma, the transport of energy and momentum, and the coupling of the ionosphere with the magnetosphere and the atmosphere (Nishimura et al., 2021). Subauroral Ion Drift (SAID) flow channels, a specific type of flow channel occurring in the subauroral region of the ionosphere, are narrow latitudinal channels of fast westward flows that appear during magnetically disturbed times and typically in the evening sector. Initially termed ‘polarization jets’ by Galperin and A.G. (1974), they were later referred to as SAID by Spiro et al. (1979) and included in the generic term ‘Sub Auroral Polarization Stream’ (SAPS) by Foster and Burke (2002), Mishin et al. (2017) later argued that SAPS implied a similar generation process. The generation of SAID channels was first explained by Southwood and Wolf (1978) as sourced from a voltage generator, and later by Anderson et al. (1993) as sourced from a current generator, with the closing ionospheric currents being the main driver. Several ground-based and space-based observations (De Keyser, 1999; Anderson et al., 1991, 2001; Puhl-Quinn et al., 2007; Foster et al., 1994; W. E. Archer & Knudsen, 2018) have shown that SAID channels are characterized by elevated electron and ion temperature and a depletion in the electron density known as a trough. The low electrical conductivity in the trough plays an important role in the development of the large flow velocities that characterize SAIDs (Ober et al., 1997; Zheng et al., 2008).

Recent studies suggest that SAID channels are associated with the Strong Thermal Emission Velocity Enhancement (STEVE) aurora. STEVE, a new type of aurora discovered initially by citizen scientists (MacDonald et al., 2018), is distinct from the classical auroras. It is characterized by a narrow ribbon of light appearing at subauroral latitudes, often associated with a ‘picket fence’ of green vertical stripes. STEVE has generated considerable interest among scientists and the public due to its distinctive appearance and unusual behavior (Gallardo-Lacourt, Liang, et al., 2018; Gallardo-Lacourt, Nishimura, et al., 2018; W. E. Archer et al., 2019; W. Archer et al., 2019; Nishimura, Donovan, et al., 2020; Semeter et al., 2020), with particular interest in its optical spectra (Martinis et al., 2022; Liang et al., 2019; Gillies et al., 2019) and magnetosphere connections (Nishimura

65 et al., 2019; Nishimura, Yang, et al., 2020). Despite its striking appearance, the phys-
 66 ical mechanisms behind the STEVE emissions remain largely unresolved, but there are
 67 ideas on how it might evolve from a Stable Auroral Red (SAR) arc (Gillies et al., 2023)
 68 or how it’s continuum spectrum could be caused by N₂ vibrational excitation (Harding
 69 et al., 2020). While classic auroras are caused by collisions between precipitating charged
 70 particles and atmospheric atoms and molecules, the processes giving rise to the distinct
 71 features of STEVE are still unclear. Sparse measurements available indicate that the flow
 72 channel associated with STEVE shows velocities larger than 5km/s and an electron tem-
 73 perature higher than 10,000K at Low Earth Orbit (LEO) altitudes, suggesting it could
 74 be an extreme version of an SAID flow channel (W. E. Archer et al., 2019; W. Archer
 75 et al., 2019). This becomes an even greater challenge when the observations exceed the
 76 designed measurement range of the sensor, leading to a disconnect between theory and
 77 measurements. While 2D studies have attempted to simulate such channels (Liang et
 78 al., 2021, 2022), we include a full 3D approach capable of resolving what we find to be
 79 substantial longitudinal variations and dynamics in the flow channels. Lynch et al. (2022)
 80 showed in 3D how FAC tearing mode are a plausible explanation for the picket fence vis-
 81 ible signature.

82 The transient and relatively rare nature of STEVE presents a challenge for exper-
 83 imental measurement. Modeling has emerged as a powerful tool for investigating the be-
 84 havior of the ionosphere and its interactions with the Sun, the Earth’s magnetic field,
 85 and the lower atmosphere, including STEVE. Various modeling techniques are available,
 86 ranging from empirical methods to complex physics-based numerical simulations. Em-
 87 pirical methods, such as IRI (Bilitza et al., 2022), NRLMSIS (Emmert et al., 2021), and
 88 NEQuick (Radicella, 2009), are based on mathematical functions derived from histor-
 89 ical experimental data. However, such empirical models may not be able to simulate con-
 90 ditions in the ionosphere when STEVE is present. On the other hand, physics-based mod-
 91 els such as TIEGCM (Qian et al., 2014), GITM (Ridley et al., 2006), and SAMI3 (Huba
 92 et al., 2008) are global models with a large grid size and geographical coverage, making
 93 it difficult to simulate STEVE due to its narrow nature. The GEMINI ionospheric model
 94 (Zettergren & Semeter, 2012) can address this issue by incorporating inputs from em-
 95 pirical models and allowing for a grid size that can be adjusted to cover a smaller ge-
 96 ographical area than global models. Designed for medium to small spatial scales (200m
 97 to 10,000km), GEMINI is well-suited for simulating extreme SAID flow channels.

98 GEMINI (Zettergren & Snively, 2019) is used in the current study to simulate an
 99 extreme SAID event using a 3D grid, using inputs motivated by existing experimental
 100 measurements. It is notable, however, that the extreme temperatures and flows within
 101 STEVE create a significant gap between observations and theory/modeling and, indeed,
 102 create some additional challenges with various parameters used in physics-based mod-
 103 els. While relatively sparse extreme SAID observation still serve as a valuable starting
 104 point for the modeling process. GEMINI is driven by a constant current density shaped
 105 by previous STEVE measurements (Nishimura, Donovan, et al., 2020). The E-region is
 106 of particular interest as there are no direct measurements that can elucidate the processes
 107 dominating the ionosphere in these extreme cases.

108 Our results show flows and current from an extreme SAID channel and how these
 109 exceed existing current measurements of STEVE. The simulations have revealed com-
 110 plex structures and behaviors, emphasizing the importance of 3D simulations in captur-
 111 ing these phenomena. The interplay between plasma depletion, conductance increase,
 112 and channel velocity increase is confirmed, even in the extreme values of 12km/s. The
 113 study has also highlighted the role of various factors, such as current density and lon-
 114 gitudinal length, in influencing the behavior of the channel velocity. However, these sim-
 115 ulations should be viewed as approximations due to the limited experimental observa-
 116 tions available to constrain the model inputs and the assumptions made to achieve sen-
 117 sible results. We are exploring behaviours at the limits of current simulations, with val-

118 ues that escape the existing formula and models for ionospheric parameters and whether
 119 these effects occur physically is not known.

120 The paper is structured as follows: Section 2 details the model setup, describing
 121 the ionospheric conditions used as inputs to the model and the modifications made to
 122 accurately simulate the behavior of an extreme SAID channel. The results of a 3D sim-
 123 ulation obtained from GEMINI are presented in Section 3. Section 4 explores these re-
 124 sults and their implications, comparing them to a 2D simulation also conducted with GEM-
 125 INI. We conclude with a summary of all results and the future work ahead in Section
 126 5.

127 2 Model setup

128 The **Geospace Environment Model of Ion-Neutral Interactions** (GEMINI) (Zettergren
 129 & Semeter, 2012; Zettergren & Snively, 2019) is a versatile three-dimensional ionospheric
 130 model, specifically designed to capture a wide range of phenomena occurring at medium
 131 to small spatial scales (200 m to 10,000 km). GEMINI is designed to function in either
 132 two or three dimensions, utilizing general orthogonal curvilinear coordinates, typically
 133 a tilted dipole (Huba et al., 2000) or a Cartesian system. The model employs a fluid sys-
 134 tem of equations (Schunk, 1977; Blevy & Schunk, 1993) to describe the dynamic behav-
 135 ior of the ionospheric plasma, which is self-consistently coupled to an electrostatic treat-
 136 ment of auroral and neutral dynamo currents. The fluid system includes three conser-
 137 vation equations (mass, momentum, and energy) for each ionospheric species s relevant
 138 to the E-, F-, and topside E-regions ($s = O^+, NO^+, N_2^+, O_2^+, N^+, H^+$).

139 To accurately model an SAID channel under extreme conditions, GEMINI must
 140 be configured appropriately. Some initial conditions, such as magnetic declination and
 141 neutral compositions (determined by MSIS00), are already handled by the model for a
 142 given location. However, users input additional configuration parameters, including drivers
 143 and grid size. To drive the SAID channel in the model a user-specified current density
 144 must be used. For our case we use the measurements from the Defense Meteorological
 145 Satellite Program (DMSP) presented in Nishimura, Donovan, et al. (2020) and Nishimura,
 146 Yang, et al. (2020) as an initial reference. These DMSP measurements represent some
 147 of the best constraints available for the field-aligned currents of the STEVE/SAID chan-
 148 nel, which should aid in accurately simulating the channel dynamics.

149 From Nishimura, Donovan, et al. (2020), the DMSP measurements show a flow chan-
 150 nel velocity with a maximum velocity of 4.5km/s and temperatures reaching approxi-
 151 mately 4,500K. These measurements appear to be saturated by the maximum values the
 152 sensor can measure. Therefore, they will be used cautiously and as a reference, with our
 153 objective being to model plasma flows larger than 5km/s and temperatures hotter than
 154 5,000K. Field-aligned current density (FAC) values go as high as $1\mu A/m^2$, which will be
 155 our upper boundary target for the current density that the system will be driven with.
 156 There also exists a detached precipitation on the upward portion of the field-aligned cur-
 157 rent. Following the results of Liang et al. (2022), a precipitation profile was used on the
 158 upward portion of the current density with a maximum value of $0.5 mW/m^2$, modeling
 159 a current that is partially carried by precipitating electrons.

160 GEMINI assumes fixed potential at the lateral boundaries of the grid (Dirichlet bound-
 161 ary conditions), while the FAC at the top fo the model is effectively treated as a source
 162 term for the field-integrated potential equation (Zettergren et al., 2015). For the fluid
 163 system of equation, at the bottom boundary, conditions are taken such that $T_s = T_n$,
 164 and at the top boundary, $T_s = T_\infty$, where T_∞ is defined in the input file to the model.
 165 However, for our particular case, we are interested in analyzing the effect of the current
 166 and the channel on the ionosphere. Thus, the top boundary condition was modified to
 167 allow energy to move freely across it by setting a specified heat flux instead of T_∞ , i.e.

168 the energy equation solution was changed to incorporation Neumann conditions for elec-
 169 tron heat conduction. In our simulations, the heat flux was set to zero, so that energy
 170 can stay in the ionosphere rather than a massive amount of heat escape at the top. Ta-
 171 ble 1 provides an overview of the most important input parameters for the model.

Table 1. Basic parameters used to run GEMINI

Parameter	Value
Duration of sim	900 seconds
Output interval	1 seconds
Grid size	$512 \times 512 \times 512$ (lphi,lp,lq)
Model Latitude span	58° to 63° North
Model Longitude span	55° to 125° East
Altitude span	0 to 1000 km
Current density target	$0.6 \mu\text{A}/\text{m}^2$
MLT at the center longitude	21

172 GEMINI simulations are conducted in two steps: an initialization/equilibration phase
 173 and a “disturbance” simulation. The primary objective of the initialization phase is to
 174 establish equilibrium within the ionospheric parameters. This involves running the model
 175 for a sufficient duration, typically several hours to a day in simulation time. The result-
 176 ing equilibrium offers a snapshot of ionospheric conditions as the grid undergoes slow
 177 diurnal variations in energy inputs.

178 In the simulations conducted for the current study, GEMINI outputs are organized
 179 along three internal coordinates: the x_1 coordinate aligns with the magnetic field line,
 180 x_2 increases as the L-shell number grows, approximately in a northern direction, and fi-
 181 nally, x_3 is the zonal direction (positive east). Output data in the model native coordi-
 182 nate system is gridded onto a regular latitude, longitude, and altitude mesh for ease of
 183 visualization and analysis, allowing for a comprehensive representation of the spatial dis-
 184 tribution of the simulated parameters. In this work we specifically use magnetic latitude
 185 and longitude for our plots.

186 2.1 Current density and precipitation topology

187 To emulate the latitudinal changes in current density as shown by Nishimura, Dono-
 188 van, et al. (2020) and Nishimura, Yang, et al. (2020), Gaussian functions of opposite sign
 189 with a small difference in their mean and maximum values were employed. Equation 1
 190 presents the analytical expression of the latitudinal geometry of the current density, where
 191 lat represents the magnetic latitude. In this case, σ_{lat} , which represents the disturbance
 192 width, was chosen to be 0.02, which translates to a current density channel width at mid
 193 height of 0.5° degrees in latitude. This approach ensures that the model accurately cap-
 194 tures the dynamics of the SAID channel. Figure 1(top) shows how the shape of the cur-
 195 rent density applied. Black solid lines represents the function displayed in Equation 1,
 196 while the orange circles represent the actual GEMINI input as sampled by the grid.

$$197 \quad J_{lat}(lat) = \exp\left(-\frac{(\text{lat}-\langle\text{lat}\rangle+1.5\sigma_{lat})^2}{2\sigma_{lat}^2}\right) - \exp\left(-\frac{(\text{lat}-\langle\text{lat}\rangle-1.5\sigma_{lat})^2}{2\sigma_{lat}^2}\right) \quad (1)$$

198 Meanwhile, in the longitudinal case, a different approach was taken to generate a
 199 current density that remains constant for several kilometers before tapering to zero be-
 200 fore reaching the boundaries of the simulation. This was accomplished by using a Raised

201 Cosine window, with an analytical expression shown in Equation 2.

$$202 \quad J_{lon}(lon) = \begin{cases} 1 & : |lon| \leq \frac{1-\beta}{2T} \\ \frac{1}{2} \left[1 + \cos \left(\frac{\pi T}{\beta} \left[|lon| - \frac{1-\beta}{2T} \right] \right) \right] & : \frac{1-\beta}{2T} < |lon| \leq \frac{1+\beta}{2T} \\ 0 & : otherwise \end{cases} \quad (2)$$

203 The Raised Cosine window facilitates the generation of a smooth curve with controllable
 204 characteristics. The shape of the window is determined by a parameter, denoted as β
 205 (roll factor), where $\beta = 1$ yields a pure cosine, while $\beta = 0$ results in a square win-
 206 dows. In our case, we aimed to generate a current density profile that peaks in the center
 207 and gradually decreases towards the edges of the simulation domain in the longitudi-
 208 nal direction. To achieve this, we used $\beta = 0.15$ and a period of $T = 1/42$, which
 209 corresponds to a longitudinal extent of approximately 40° from midpoint to midpoint.
 210 The general shape is displayed in Figure 1(bottom), with the solid black line represent-
 211 ing the shape of Equation 2 and the orange circles representing the actual GEMINI in-
 212 put as sampled by the grid.

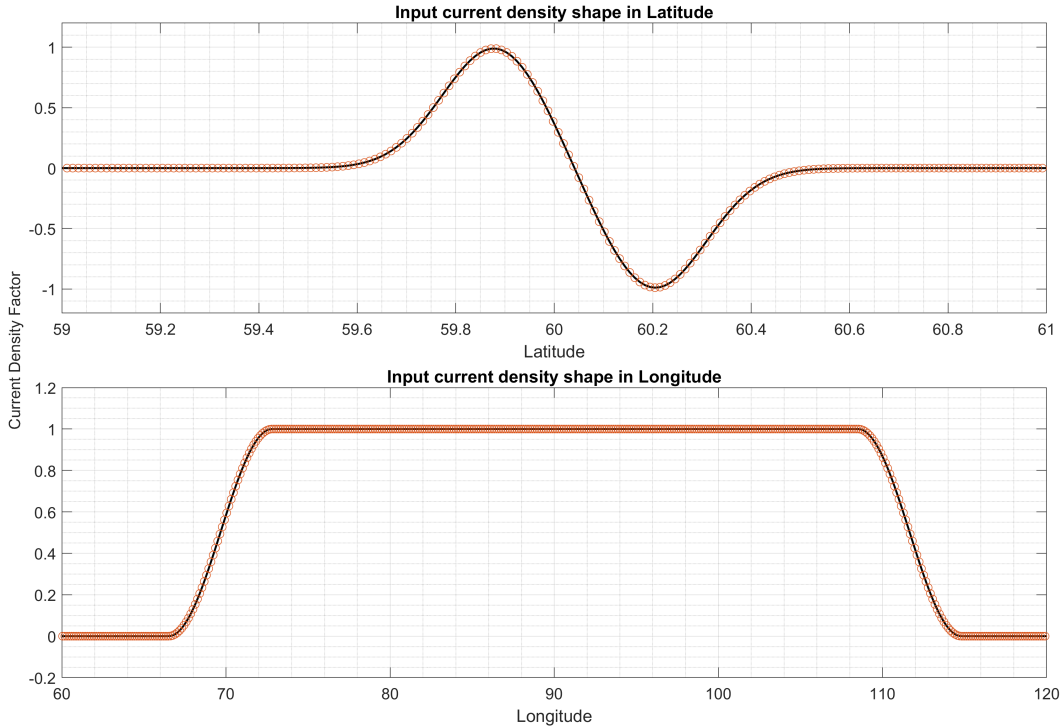


Figure 1. Riased cosine input current defined at the top layer of the grid

213 As previously stated, electron precipitation was incorporated into the model. The
 214 precipitation profile mirrors the shape of the current density in the longitudinal coordi-
 215 nate and only includes the negative Gaussian for the shape in latitude. Both the central
 216 energy and total energy flux adopt this Gaussian shape, peaking at 0.5 mW/m^2 for
 217 the total energy flux and 2 KeV for the central energy. These values were chosen follow-
 218 ing the results of Liang et al. (2022), which included this precipitation in the upward part
 219 of the current, which also shows that this can be observed in DMSP measurements (Fig-
 220 ure 7 of Nishimura, Donovan, et al. (2020)) or be inferred from the existing electron flux
 221 spectrograms (Mishin et al., 2017; Puhl-Quinn et al., 2007).

222 Our approach takes inspiration from previous works, particularly Liang et al. (2022),
 223 while it differentiates itself from these studies by including the longitudinal dimension

224 on the simulations based on the observations of Nishimura, Donovan, et al. (2020) and
 225 Gallardo-Lacourt, Nishimura, et al. (2018). On the other hand, Lynch et al. (2022) ap-
 226 plies an electric field driver, which produces a flow-induced conductance gradient, wherein
 227 the FACs adjust independently to create a self-consistent system, showing that the re-
 228 sulting current sheets may be tearing-mode unstable. By contrast, we are applying a cur-
 229 rent density driver, and allowing electric fields to adjust self-consistently. This adjust-
 230 ment involves a complex interplay between electric fields, flow velocities, ion chemistry,
 231 plasma depletion, and plasma temperatures. We expect the time-dependent development
 232 of the channel pushes key parameters up to and beyond their range of applicability and,
 233 indeed, limitations in the physical descriptions used in GEMINI. Our use of a current
 234 density driver could be argued as more realistic than an electric field driver, since the
 235 stored energy in the magnetosphere is expected to be inductive in nature, although both
 236 approaches have assumptions and limitations. Ultimately what might be needed is an
 237 Alfvénic boundary condition inside GEMINI, as discussed in Wright and Russell (2014).
 238 At the same time we will focus on the chemical processes in the E-region, something not
 239 shown by Lynch et al. (2022).

240 **2.2 Changes to GEMINI Required to Accommodate Extreme Condi-** 241 **tions**

242 Since we simulate an extreme SAID channel, where velocities are expected to ex-
 243 ceed 5 km/s, several adjustments must be made to the model to accommodate the an-
 244 ticipated extreme temperatures (above 30,000 K). Most of these adjustments are directly
 245 related to results obtained from laboratory experiments or other data, which are often
 246 fitted to relatively simple functional forms that can produce nonsensical results (e.g. neg-
 247 ative collision frequency) when applied outside their domain of applicability. In the course
 248 of conducting the simulations for this study we found a number of such parameteriza-
 249 tions that apparently break down for extreme ion or electron temperature values.

250 GEMINI values for electron-neutral momentum transfer collision frequencies were
 251 sourced from Schunk and Nagy (2009), who directly references Itikawa (1974). The lat-
 252 ter obtained the momentum transfer cross-section for electron collisions from laboratory
 253 experiments and theoretical data. For simulation of extreme conditions the electron-N₂
 254 collision frequency (equation 3) and the electron-H collision frequency (equation 4) pose
 255 a challenge since they are not positive-definite for arbitrary values of temperature (i.e.
 256 T_e).

$$257 \nu_{e-N_2} = 2.33 \times 10^{-11} n(N_2) (1 - 1.21 \times 10^{-4} T_e) T_e \quad (3)$$

$$258 \nu_{e-H} = 4.5 \times 10^{-9} n(H) (1 - 1.35 \times 10^{-4} T_e) T_e^{1/2} \quad (4)$$

260 In this work, to prevent negative collision frequencies, the electron temperature is
 261 capped at a value 1000 K lower than the temperature at which the collision frequency
 262 crosses zero at approximately 7,000 for the electron-N₂ collision frequency and 8,000 for
 263 the electron-H collision frequency. This is done only for purposes of computing problem-
 264 atic quantities and allows the electron temperature to rise above that value, but a max-
 265 imum fixed value is used in the calculations of the electron neutral collision frequencies.
 266 Ion-neutral collision frequencies do not face the same issue as their functional form is $(A -$
 267 $B \log_{10}(\frac{T_i + T_e}{2}))^2$. Given this characteristic, no modifications were needed for ion-neutral
 268 collision frequencies.

269 Since the collision frequencies between electrons and some neutrals are affected, elec-
 270 tron thermal conduction, which governs electron heat flow, is also impacted. Equation
 271 5 shows the thermal conductivity directly taken from Schunk and Nagy (2009), which,
 272 in turn, references Banks (1966). Since this equation depends on the average of the mo-
 273 mentum transfer cross-section ($\langle\langle Q_{en}^{(1)} \rangle\rangle$) between electrons and neutrals, it faces similar

274 issues mentioned with electron-neutral collision frequencies. The electron-N₂ cross-section
 275 is given by $Q_{eN_2}^{(1)} = 2.82 \times 10^{-17} (1 - 1.21 \times 10^{-4} T_e) T_e^{1/2}$. Therefore, the electron ther-
 276 mal conductivity is also capped in the same fashion – at a temperature below the point
 277 where the function crosses zero for this particular calculation.

$$278 \quad \lambda_e = \frac{7.7 \times 10^5 T_2^{5/2}}{1 + 3.22 \times 10^4 \frac{T_e^2}{n_e} \sum_n n_n \langle Q_{en}^{(1)} \rangle} \quad (5)$$

279 Another set of calculations that became problematic in our simulations at large tem-
 280 peratures is electron energy losses due to vibrational excitation of N₂ and O₂. As de-
 281 scribed by Pavlov (1998), the [N₂] rotational losses have a rather complicated analyt-
 282 ical expression which is only valid for values of electron temperature between 300K and
 283 6,000K. Similarly, Jones et al. (2003) results show how the [O₂] vibrational losses are only
 284 valid for values of electron temperature between 300K and 6,000K. One might be tempted
 285 to utilize these functions above 6,000K, but since these two vibrational losses are log-
 286 arithms of polynomial fittings, their behavior outside of the range of 6,000K is of an un-
 287 bound growth. As such, all electron temperatures were capped at 6,000K when calcu-
 288 lating vibrational losses. Additionally vibrational rates in the 300-6000 K range were up-
 289 dated to include the most recent work on these topics (Schunk & Nagy, 2009)

290 GEMINI also required some changes to the numerical solvers to obtain stable re-
 291 sults at extremely large flows and temperatures. Normally GEMINI will resolve the tem-
 292 perature equation as a series of operator splits that individually resolve substeps of (a)
 293 advection, (b) compression, (c) thermal conductivity, and (d) source-loss terms. We have
 294 found that these different terms are best resolved in order of increasing numerical stiff-
 295 ness – in normal conditions for the ionosphere in the order listed above. However, at very
 296 high temperatures the thermal conduction and complicated source-loss process essen-
 297 tially compete for control of the temperature. In this case we have found that artificial
 298 oscillations in time can result unless one resolves numerical substeps c and d *simulta-*
 299 *neously* so they may balance each other instantaneously in the code. Thus, we have found
 300 it necessary in our simulations to solve both thermal conduction and energy source loss
 301 terms together in a single substep. For this study, we use either a TRBDF2 (LeVeque,
 302 2007) or backward Euler numerical solutions for the resulting diffusion-reaction type equa-
 303 tion. This is in contrast with the standard GEMINI approach of resolving a diffusion equa-
 304 tion with TRBDF2 and feeding the result into a reaction equation that uses an expo-
 305 nential time differencing scheme (a split operator approach).

306 **3 Simulation results for an extreme SAID channel**

307 **3.1 3D simulation**

308 In this section, we present the results of our 3D simulations of an extreme SAID.
 309 We focus only on a portion of the simulation outputs, with the a complete set of out-
 310 puts ($N_s, v_{1-3}, T_s, J_{1-3}, E_{2-3}, \sigma_P, \sigma_H$) available as Figures and Movies in the supporting
 311 material (Figure S1 - S19, Movie S1 - S17). Our main focus will be on the spatial and
 312 temporal variations of the plasma density ([Ne],[NO⁺],[O⁺], and [O₂⁺]), ion and electron
 313 temperature (T_i and T_e), closure current (J₂), and channel velocity (v₃), which are key
 314 parameters to characterize the SAID phenomenon.

315 Figure 2 displays simulation results, focusing on field-aligned profiles at the flow
 316 channel center in both latitude and longitude. It particularly highlights the channel ve-
 317 locity, the driving and closure current, as well as the ion and electron temperature. The
 318 center in latitude is defined as the location of zero FAC between the upward and down-
 319 ward current density (J₁), where temperatures and densities undergo the most drastic
 320 changes. The center in longitude is defined as 90°.

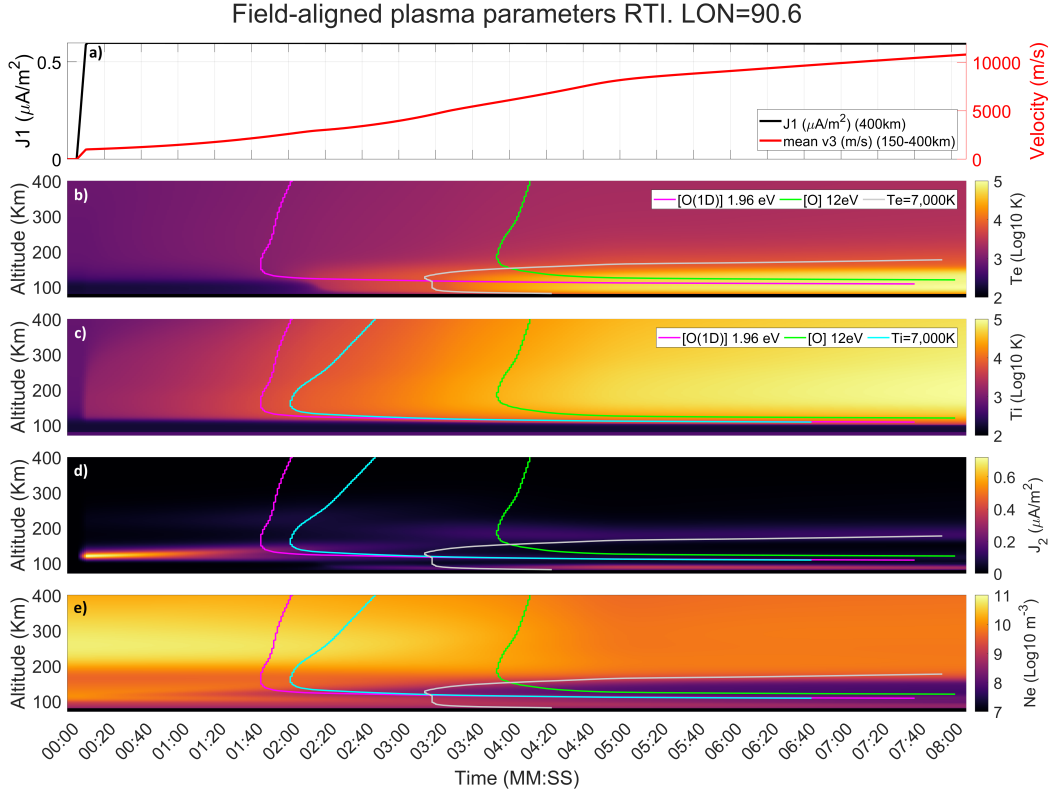


Figure 2. Field-aligned profiles are taken at the center of the flow channel. Panel a) displays values for parallel-to-B current density (J_1) and east/west velocity (v_3) averaged from 150 to 400 km. Panels b) and c) show electron (T_e) and ion (T_i) temperatures in Log10 scale. Panel d) depicts the north/south current (J_2), while panel e) provides insights into the total electron density (N_e)

321 The extra lines included in panels a) through e) represent points in time and alti-
 322 tude where a model parameter surpasses a certain threshold where physics not included
 323 in the model could start taking effect. The magenta represents the point where the total
 324 energy (kinetic + thermal) of $[O_2^+]$ reaches the energy needed to trigger the first excited
 325 state of $[O]$, $O(^1D)$, at 1.96eV. The green line on the other hand is the point where
 326 the total energy of $[O_2^+]$ reaches the energy needed to ionize $[O]$, at 12eV, with $[NO^+]$
 327 reaching the same threshold just a second or two after due to its marginally smaller atomic
 328 mass. Finally, the cyan and gray lines represent the points in time and altitude where
 329 the ion and electron temperature reach 7,000K, respectively. 7,000K is an important tem-
 330 perature, since many equations are only valid until that point, even if they do not cause
 331 the model to break due to unexpected negative values. For the ion temperature this only
 332 applied currently to the losses due to the vibrations and rotational modes of $[N_2]$ and
 333 $[O_2]$. Most ion-neutral collision frequencies are also defined up to this threshold, but since
 334 their dependence is mostly Log10 with temperature, extending to larger temperatures does
 335 not cause large issues. For the electron case, it is the point where some electron-neutral
 336 collision frequencies are capped as explained in 2.2, as well as marking the top bound-
 337 ary where other uncapped electron-collision frequencies are valid. This will be impor-
 338 tant further on, since for large temperature these electron-neutral collision will grow lin-
 339 early with temperature. Figure S1, S6, S11, and S16 in the supporting material show these
 340 thresholds and the energy of $[O_2^+]$ for further analysis.

Figure 3 serves as a companion to Figure 2, focusing specifically on channel velocity, temperatures, specific ion densities, growth rates in velocity and temperature, as well as height-integrated conductivity. Analogue to Figure 2, the magenta, green, and cyan lines represent the same thresholds mentioned above, with the black line replacing the gray one for better visibility.

In the initial 5 seconds of the simulation, no current driver is applied. J_1 grows linearly over the next 5 seconds to a value of approximately $0.6 \mu\text{A}/\text{m}^2$ at an altitude of 400km, and remains constant for the rest of the simulation, as shown in panel a) of Figure 2. During this brief time frame, the channel velocity increases to 1km/s at 00:10. A shorter growth time for the driving current was chosen to isolate the effects of a large current driving the extreme channel. The east/west velocity of the channel (v_3) is also displayed in Figure 2a), revealing a changing slope. The distinctions between different time phases become more apparent in Figure 3, from which we can identify four different phases.

The first phase, from 00:10 to approximately 02:10, there is an exponential increase in the channel velocity v_3 , starting from 1 km/s and ending with 2.7 km/s at the 02:10 mark. This increase is accompanied by a growth in both electron and ion temperatures, with the ion temperature remaining below 7,000 K and the electron temperature below 3,000 K, as depicted in Figure 3a). The growth in ion temperature coincides with the growth in channel velocity, as they are related, as explained by St-Maurice et al. (1999).

Two important thresholds are reached at approximately the 01:40 minute mark. First, the ion temperature is now high enough for the reaction $[O^+] + [N_2] \rightarrow [NO^+] + [N]$ to accelerate as the temperature increases. This implies that most of the $[O^+]$ in the lower F-region will be converted to $[NO^+]$ (St-Maurice & Laneville, 1998). Second, $[O_2^+]$ has enough energy to trigger inelastic collisions that excite $O(^1D)$. Therefore the two main ions in the E- and lower F-region will start to lose some of their energy to this inelastic process that is not included in GEMINI, reducing the channel velocity without affecting the electric field. This will affect plasma from 110km and above. Inelastic collisions can be considered the first factor not included in GEMINI that will stop the growth of the channel velocity.

The primary closing current (J_2) occurs between 110 km and 130 km, as seen in Figure 2d). On the other hand, the density, as shown in Figure 2e), is gradually starting to deplete, with the first signs appearing around the 00:30 second mark.

The depletion of plasma in the E-region, where most of the current is closing, leads to a decrease in the Pedersen conductivity. To maintain a constant driving current, this, in turn, necessitates an increase in the poleward electric field within the channel, meaning an increase in the channel velocity. The layer of the closure current J_2 , as depicted in Figure 2d), also spreads to a higher altitude due to the loss of the E-region density. When we compare this information with Figure 3b), we observe that the first phase concludes approximately when the acceleration reaches a local maximum. The local minima achieved right after the end of the phase coincides with point where the ion temperature reaches 7,000K, the threshold marked by the cyan line.

Figure 3c) displays the densities of the main ion species ($[NO^+]$ solid black line, $[O_2^+]$ solid blue line, and $[O^+]$ solid red line). We note that the first phase is characterized by a continuous growth of $[NO^+]$ and a subsequent decrease of $[O^+]$ at 240 km, which is expected since the ion temperature is sufficiently high for that reaction to occur. Concurrently, the densities at 120 km are steadily decreasing (black and blue dashed lines). The local maximum appears to align itself to a point where $[NO^+]$ and $[O^+]$ are comparable. Finally, Figure 3d) illustrates how the total Pedersen conductance (solid black line) rapidly decreases during this first phase, becoming 32% of its original value by the

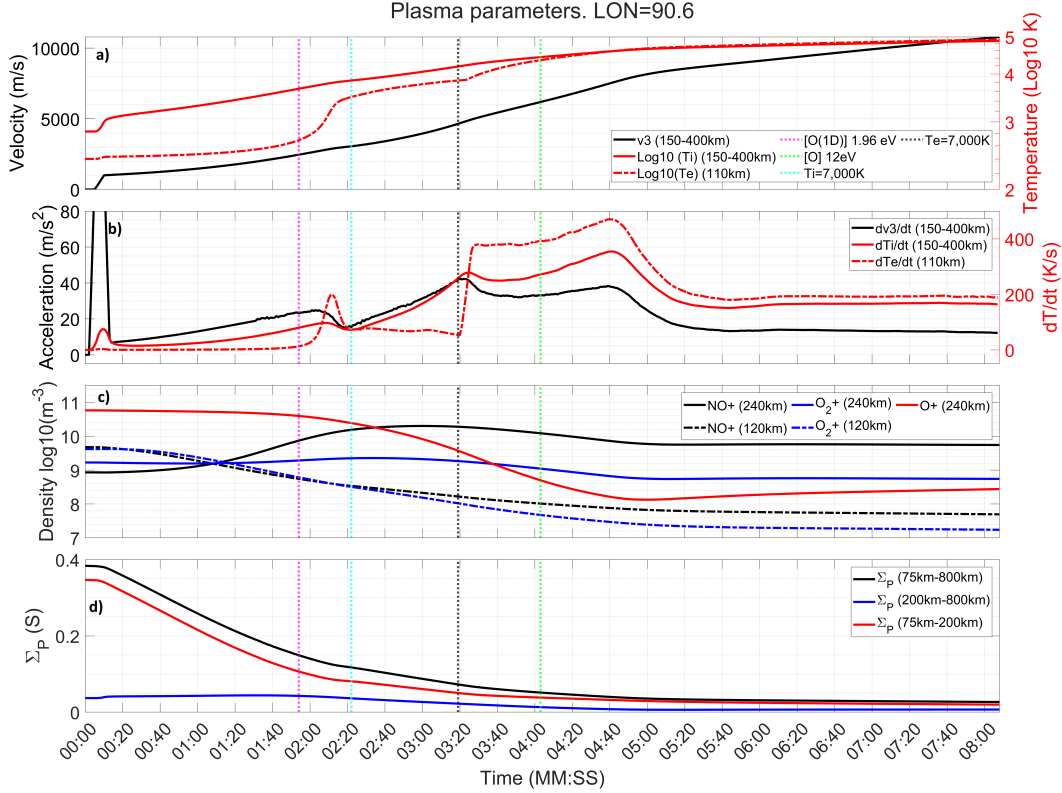


Figure 3. Key simulation output parameters. Panel a) shows the average channel velocity (v_3 , solid black line) and ion temperature (T_i , solid red line) in Log10 scale between 150-400km, as well as the electron temperature (T_e , dashed red line) at 110km. Panel b) shows the time derivative of all variables shown on panel a). Panel c) shows the density of the main ions, $[NO^+]$ and $[O_2^+]$ at 120km (black and blue solid lines) and 240km (black and blue dashed lines) as well as $[O^+]$ at 240km (solid red line). Panel d) shows the total height integrated Pedersen conductance (Σ_p , solid black line), as well as the F-region (200-800km, solid blue line) and E-region (95-200km, solid red line) contribution

391 02:10 minute mark. Most of this change is attributed to the E-region conductance (solid
 392 red line) as the plasma gradually depletes in the area.

393 The second phase occurs between the two local maxima (02:10 and 03:20), as depicted in Figure 3b), where abrupt changes to the acceleration occur, reaching a maximum of 40 m/s² by the end of the phase, with a final channel velocity of 4.8 km/s. During this same period, the electron temperature remains below 7,000 K, while the ion temperature rises to 15,000 K. Even though the electron temperature has not reached the point where it goes beyond 7,000K, there is a particular phenomena happening between 02:10 and 02:20 where there is a sudden change to the temperature, jumping from approximately 700K all the way to 2,500K in a span of 10 seconds. This change is also visible in the growth rate of electron temperature. The reason for this is frictional heating due to the large electric field, that reaches a value of 200mV/m at the 02:10 minute mark. From the Supporting Movie MS03 it is possible to see how this enhancement goes from 150km to 100km. Due to the enhanced electric field, the frictional heating at these altitudes is now considerable and thus triggers this enhancement of electron temperature.

406 The most significant changes are observed with the closing current and the total
 407 plasma density, as shown in Figure 2d) and e), with the current dividing into several smaller
 408 channels as the density in the E-region becomes entirely depleted. The end of the phase
 409 coincides with the point where the electron temperature reaches 7,000K, and so our electron-
 410 neutral collision frequencies from now on are outside of the bounds of their respective
 411 equations.

412 This can be considered a transition phase in terms of closure current, with a small
 413 amount of current still flowing through the E-region. However, since the plasma in that
 414 area is constantly being depleted, some current is now flowing through the lower F-region
 415 and at an altitude of 100 km. The increase in electron temperature to such high values
 416 is directly attributed to the frictional heating term in the energy equation for the elec-
 417 trons ($Q_e = m_e \nu_e n_0 E^2 / B^2$). This enhanced electron temperature extends down to 85
 418 km and causes the electron-neutral collision frequency to rise to a value comparable to
 419 the local electron cyclotron, thus enabling electrons to carry a Pedersen current at an
 420 altitude of 100 km. The inelastic collision that should have trigger on the previous phase
 421 will also have the effect of decreasing the frictional heating by soaking up energy out of
 422 the plasma. This also explains why the phase ends with a decrease in acceleration as well
 423 as a slower decrease in the Pedersen conductance, since there is some small conductiv-
 424 ity being generated by these collisional electrons.

425 Figure 3c) illustrates how the density at 240 km of $[O^+]$ rapidly decreases during
 426 this period. On the other hand $[NO^+]$ slows its increase, reaching a maximum of $2 \times$
 427 10^{10}m^{-3} . This can be attributed to the recombination of $[O^+]$, which becomes almost
 428 completely depleted, preventing the reaction from occurring at a higher rate. The bound-
 429 aries of this phase also align with the points where $[O^+]$ becomes comparable to $[NO^+]$
 430 at the beginning, and where it becomes comparable (within an order of magnitude) to
 431 $[O_2^+]$ at the end. At 120 km, we observe the densities rapidly decreasing at an exponen-
 432 tial rate. The total conductance in Figure 3d) steadily decreases just as before, with the
 433 E-region once again being the main contributor to this decrease, although the F-region
 434 does see some decrease. As such, the rapid increase in acceleration and temperature can
 435 be readily explained by the plasma being primarily depleted in the E-region, with a mi-
 436 nor contribution from the F-region. Since this section ends with the point in time where
 437 the electrons reach 7,000K, the electron-neutral collision frequencies are still valid dur-
 438 ing this period.

439 The third phase exists between the second set of local maxima, starting at 03:20
 440 and ending at 04:40. It is possible to see how right after the end of the second phase,
 441 which coincides with the point where the electron temperatures reaches 7,000K, there
 442 is an explosive growth of the temperature and an intensification of the current density
 443 at 100km. This happens because a decision was made not to cap the temperature when
 444 calculating the collision frequencies unless absolutely necessary, since one of our objec-
 445 tives is to show and make evident that the collision frequencies commonly used in SAID
 446 modeling are not valid under the extreme conditions of SAID-STEVE events. These col-
 447 lision frequencies applied in our simulations can grow unbounded, causing the electron
 448 frictional heating term to grow in the same manner. The positive feedback of a large and
 449 growing electric field and the collision frequencies depending on the temperature itself
 450 causes the frictional heating between 100 to 150 km to skyrocket, particularly caused by
 451 the collisions between electrons and $[O_2]$.

452 This phase is where the maximum growth of the channel velocity occurs, starting
 453 at a velocity of 4.7 km/s and ending with 7.5 km/s as seen in Figure 2a). This period
 454 also shows significant increases in ion temperatures. From Figure 3b), we can see that
 455 the acceleration reaches up to 40m/s^2 , the ion temperature growth increases up to 350
 456 K/s, and the electron temperature experiences the largest growth rate at 470 K/s. By
 457 the end of the phase, electrons at an altitude of 110 km have reached a temperature of
 458 38,000 K, with the average ion temperature between 150 and 400 km reaching the same

459 value. The reaction between $[O^+]$ and $[N_2]$, which was extended to 70,000 K by Liang
 460 et al. (2021), is still valid during this phase.

461 Another milestone is reached during this phase, since $[O_2^+]$ reaches 12eV at the 04:00
 462 minute mark. As seen on 2e), we see how there is a sizeable portion of the E-region that
 463 will have ions with energies large enough to ionize the neutral $[O]$ in the atmosphere. As
 464 such, there will be an increase in plasma from 120km up caused by impact ionization from
 465 this point on. This means that the conductance will start to increase during this time
 466 frame for the same altitude range, decreasing the need for such a large electric field and
 467 lowering the channel velocity. Impact ionization can be considered the second factor not
 468 included in GEMINI that will stop the growth of the channel velocity.

469 The two time limits of the phase also roughly coincide with two milestones in the
 470 plasma density as seen in Figure 3c). The 03:20 mark is where the density of $[O^+]$ at 240
 471 km becomes comparable with the density of $[O_2^+]$, whereas the 04:40 mark is where $[O^+]$
 472 reaches values comparable to the densities of $[NO^+]$ and $[O_2^+]$ in the E-region, at an al-
 473 titude of 120 km. From Figure 3d), we see that the conductance has reached a value of
 474 0.03 S, less than 10% of its original value of 0.38 S.

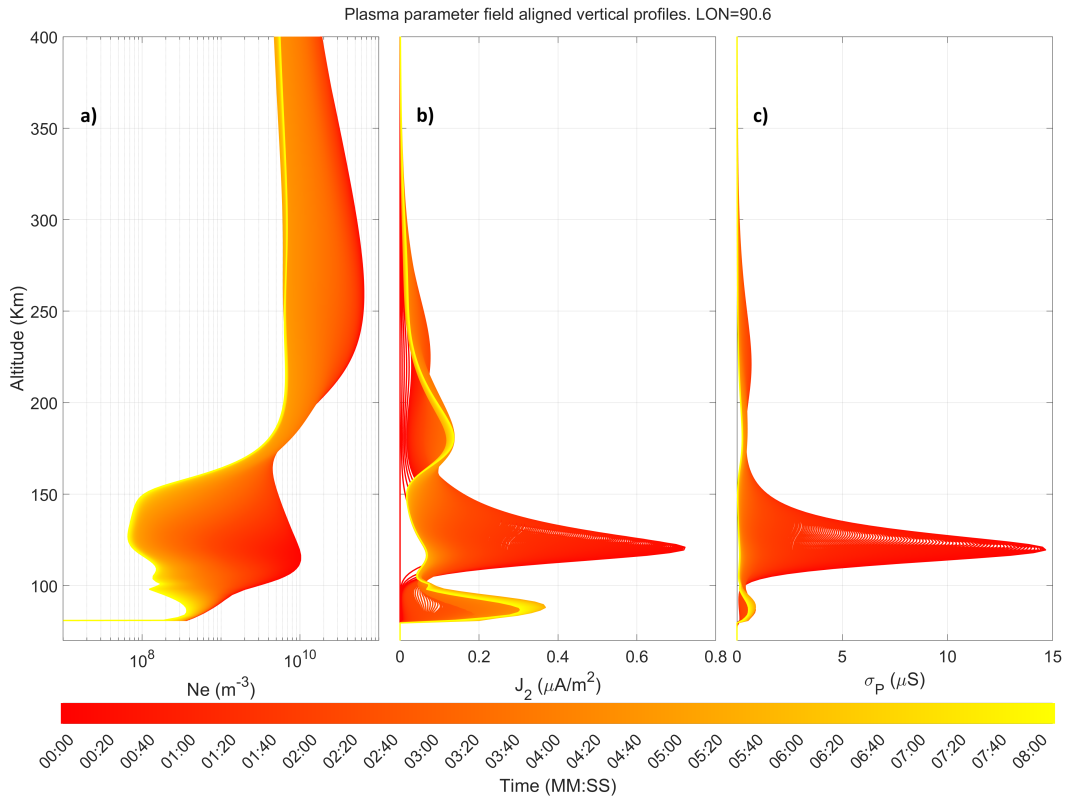


Figure 4. Field-aligned plasma parameters. Time is represented as a gradient from red to yellow as seen on the bottom bar. Panel a) plasma density at the center of the channel. Panel b) closure current density (J_2) at the center of the channel. Panel c) Pedersen conductivity at the center of the channel.

475 The final phase takes from 04:40 to 08:00. As depicted in Figure 2a), the channel
 476 velocity grows at a constant rate, with Figure 3b) confirming an almost constant accel-
 477 eration of 14 m/s², reaching a maximum value by the end of the simulation. The ion and
 478 electron temperatures also increase linearly, as seen in Figure 2b)-c) and 3a)-b). From

479 Figure 2d), we observe that the current density in the 110 to 130km altitude range is al-
 480 most non-existent, with most of the current flowing either in a narrow band at 100 km
 481 or a wider band at 180 km. The plasma density in the E-region reaches values below 10^8
 482 particles/m³, as seen in Figure 2e) and 3c). This final phase is characterized by a con-
 483 stant value of $[NO^+]$ and $[O_2^+]$ at 240 km, with a slight increase in the density of $[O^+]$.
 484 In the F-region, the plasma density is slowly decreasing. Finally, the conductance reaches
 485 a minimum value of 0.02 S, as seen in Figure 3d).

486 Figure 4 depicts the temporal changes in plasma density (panel a), closure current
 487 (panel b), and Pedersen conductivity (panel c) at the center of the flow channel. The
 488 progression of time is color-coded from red to yellow, as shown at the bottom of the fig-
 489 ure. This display provides a better representation of the quantitative variations in pa-
 490 rameters. Panel a) reveals a continuous depletion of plasma density at all altitudes through-
 491 out the lifespan of the channel, particularly at 130 km. Here, the density decreases un-
 492 til it reaches a minimum of $6 \times 10^7 \text{m}^{-3}$, corresponding to an extremely low value of 60
 493 particles/cm³.

494 Figure 4b) and 4c) provide insight into how the changes in conductivity and clo-
 495 sure current correspond to the behavior of the plasma density. Initially, most of the cur-
 496 rent flows at 120 km, decreasing rapidly as time progresses and the conductivity dimin-
 497 ishes. Towards the end of the simulation, the conductivity is nearly 0 between 100 and
 498 130 km, forcing the current to flow from 140 km upwards to 300 km, with a peak at 180
 499 km. The existence of density and extreme temperatures below 100 km contribute to the
 500 conductivity in the area, which is why we see current flowing below 100 km. This cur-
 501 rent grows with time, but after reaching a maximum value of $0.36 \mu\text{A}/\text{m}^2$, it starts de-
 502 creasing, as does the plasma at that altitude.

503 The simulation spans over 40° in longitude, making it crucial to address the dif-
 504 ferences in longitude in the flow channel. Both Nishimura, Donovan, et al. (2020) and
 505 Gallardo-Lacourt, Nishimura, et al. (2018) set the length in longitude to be close to the
 506 value we utilize. Figure 5 displays both the average channel velocity from 150 to 400 km
 507 at the center of the channel and parallel to the magnetic field lines in the top panel, and
 508 the average channel acceleration between the same locations in the bottom panel. The
 509 Y-axis represents the longitude. Since the center of the channel is at 21 MLT, the larger
 510 the longitude, the further we are from the subsolar point.

511 Figure 5a) illustrates how the channel velocity grows faster at larger longitudes from
 512 00:20 to 03:00. This is an expected result, since due to the day/night cycle of GEMINI,
 513 the eastern side will have less plasma density due to recombination in the absence of the
 514 dayside photoionization; i.e. this part of the channel has been in darkness longer than
 515 the western portion. The threshold for the energies and temperature previously defines
 516 also have the same behavior, starting first on the eastern side and later on towards the
 517 west. The cyan line, representing the point where the ion temperature reaches 7,000K,
 518 coincides perfectly at all longitudes with the minimum value of channel acceleration, and
 519 thus close to the end of the first phased defined before.

520 From 03:00 to 06:00, the maximum channel velocity travels from the eastern side
 521 towards the western side, finishing with somewhat uniform channel velocity along lon-
 522 gitudes, but with a peak in the far west. From panel b), the acceleration shows us how
 523 the different phases that were mentioned before exist in longitude, with Figure 3 being
 524 a cut at the 90.6° in longitude. On the eastern side, there is a peak-valley-peak con-
 525 figuration, which differs from Figure 3 where there were three distinct peaks in the accel-
 526 eration. The first peak-valley-peak configuration has this “travel” behavior, where it starts
 527 first on the eastern side and “travels” to the western side as time goes on. The first peak
 528 is also more pronounced towards the east and almost disappears towards the west. The
 529 second peak has a similar behavior, with it being more pronounced on the eastern side,
 530 though it remains constant in magnitude as we move closer to the west. Following the

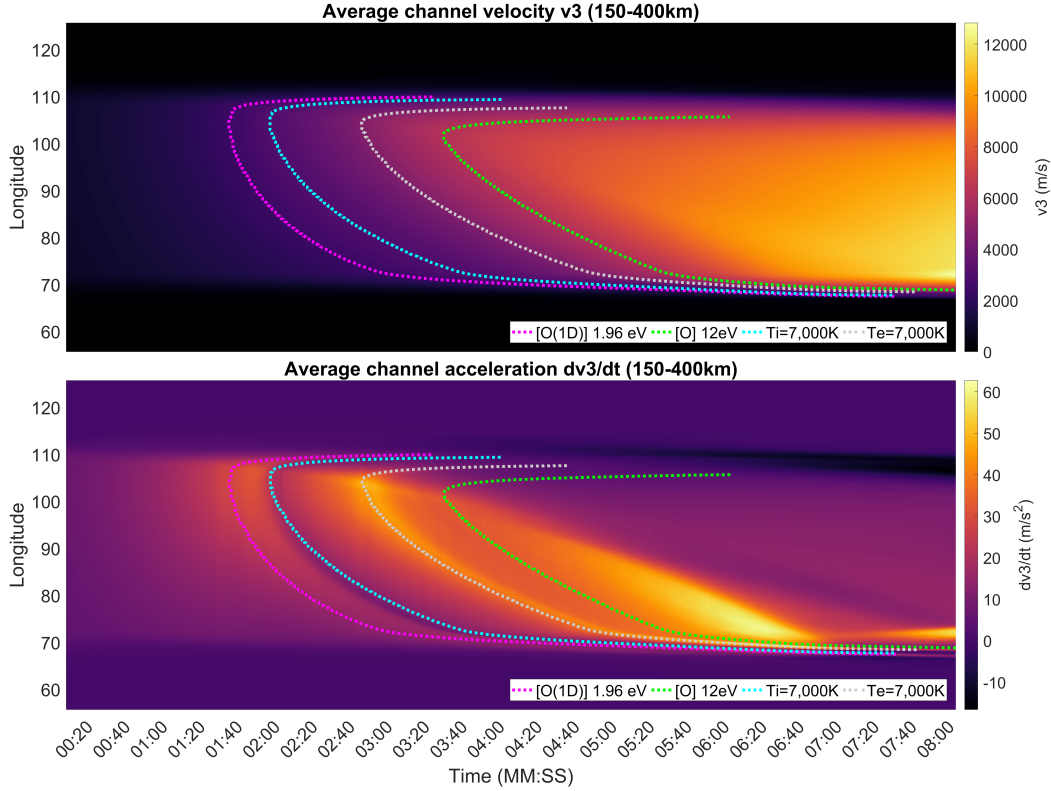


Figure 5. Average channel velocity (top panel) and acceleration (bottom panel) between 150-400km. Y axis represents longitude at the center of the channel. Simulation starts when the 90° longitude point reaches 21 MLT. Threshold lines are also included

531 same east to west motion, we see how the first peak and valley take longer to appear the
 532 westwards we are. Once again, we have a perfect alignment of this second high peak in
 533 acceleration with the point in time where the electron temperature reaches 7,000k (gray
 534 line).

535 The third peak in acceleration starts to show up at approximately 95° , with it be-
 536 coming more pronounced the further westward we go. By focusing on the changes in den-
 537 sity at these two altitudes with longitude at the center of the channel, we can gain fur-
 538 ther insights. Figure 6(top) illustrates how the total plasma density at 120 km changes
 539 over time at the center of the channel in longitude, while Figure 6(bottom) shows the
 540 total plasma density at 240 km. It's evident that the density depletion at 120 km fol-
 541 lows the same pattern as the average channel velocity as seen in Figure 5(top). The de-
 542 pletion is faster on the eastern side at the beginning, with the maximum depletion zone
 543 moving from east to west as time progresses. By the end of the simulation, the western
 544 side is slightly more depleted than the eastern side at 120 km, which directly correlates
 545 to the slightly larger velocity in the same area.

546 As for the density at 240 km, we observe that it takes much longer for depletion
 547 to occur, and the depletion is not as extreme as it is lower in the ionosphere. However,
 548 it still approaches a decrease of one order of magnitude in the western side by the end
 549 of the simulation. This also exhibits the same behavior in terms of where the depletion
 550 starts, being depleted first on the eastern side, while the west becomes much more de-
 551 pleted but later in time. This confirm that that the final peak happens due to an marge

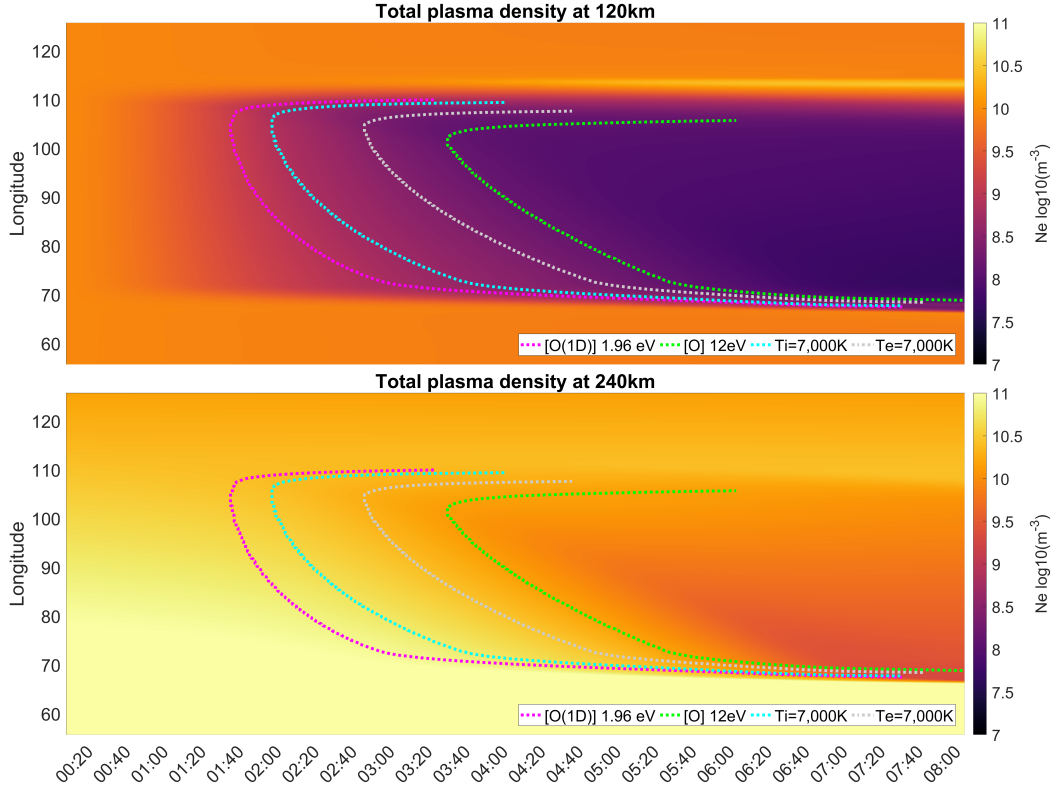


Figure 6. Total plasma density at 120km (top) and 240km (bottom). Y axis represents longitude at the center of the channel. Simulation starts when the 90° longitude point reaches 21 MLT

552 larger depletion of plasma, since the western portion of the F-region sees a much larger
 553 depletion than its eastern counterpart.

554 Even though the F-region plasma density does not have a significant impact on the
 555 channel velocity when compared to the E-region plasma density, the gradient in F-region
 556 density from east to west contributes to the “travel” behavior of the average channel ve-
 557 locity. These results underscore the complex interplay between various factors in influ-
 558 encing the behavior of the channel velocity.

559 Examining snapshots of the 3D volume at different times can provide valuable in-
 560 sights into the evolution and shape of plasma parameters under the influence of a con-
 561 stant current density driver. Figure 7 and 8 display the total plasma density at 03:00
 562 and 07:00 minutes, respectively. Each figure is divided into four panels: panel a) pre-
 563 sents a latitudinal cut at the center longitude of the flow channel, panel b) provides a longi-
 564 tudinal cut along the magnetic field line, and panels c) and d) offer altitude cuts at 120
 565 km and 240 km, respectively. These figures illustrate how the plasma density on the north
 566 side is enhanced by the precipitation on the upward part of the current density, and how
 567 the depletion at the center of the channel is concentrated between 100 and 150 km. The
 568 channel’s behavior on the longitudinal coordinate is somewhat uniform, but with a taller
 569 plasma depletion on the eastern side. The plasma depletion spans the entire longitudi-
 570 nal length at 120 km, with the depletion somewhat choked at the eastern edge. At 240
 571 km, the plasma depletion is yet to be significant. Supplementary material, including movies
 572 showing all plasma parameters (Movie S1-S17), is available for further examination.

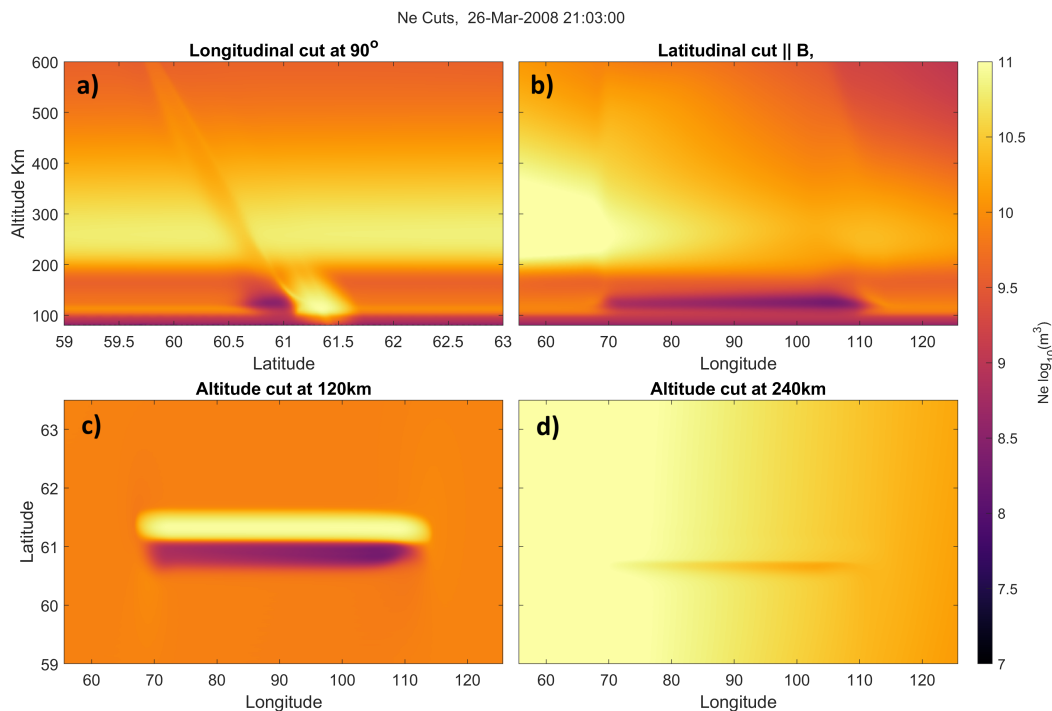


Figure 7. Plasma density at 03:00. Panels a) is a cut in longitude at 90° . Panel b) in cut in latitude along the magnetic field line. Panels c) and d) are altitude cuts at 120km and 240km.

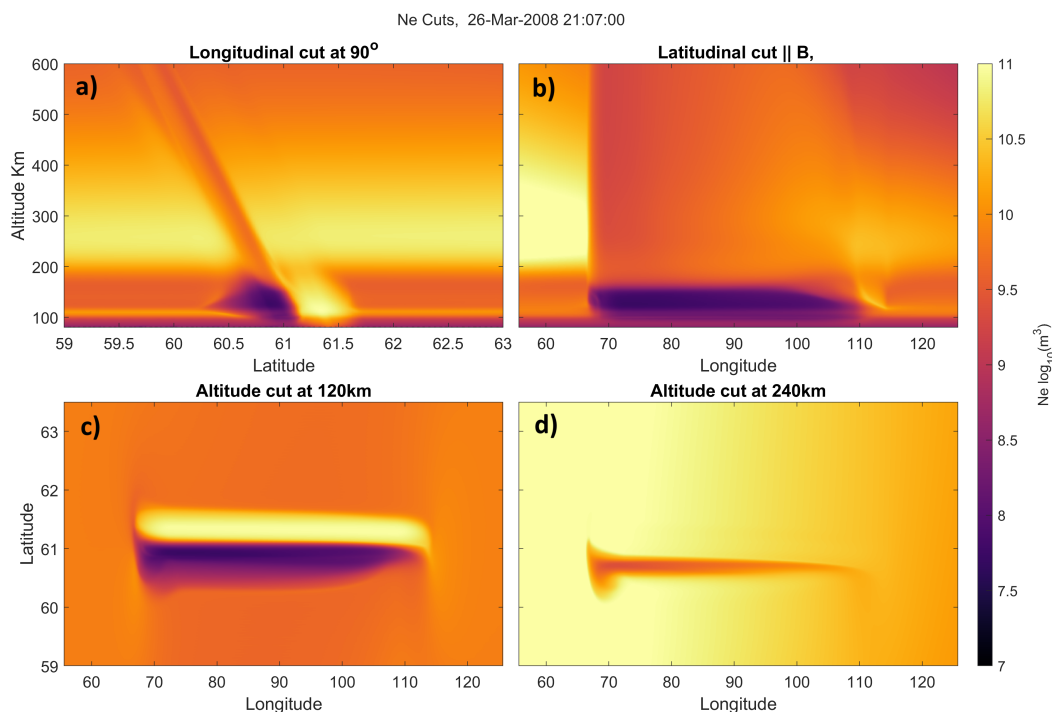


Figure 8. Plasma density at 07:00. All locations in latitude, longitude and altitude are the same as the ones shown on Figure 7

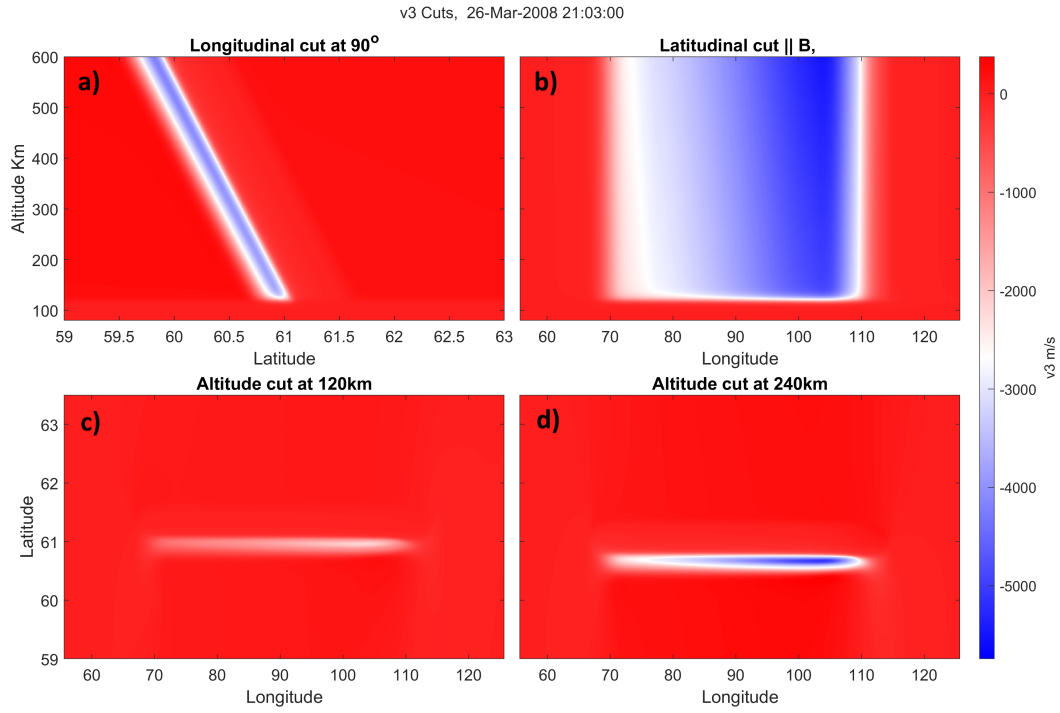


Figure 9. Channel east-west velocity at 03:00. All locations in latitude, longitude and altitude are the same as the ones shown on Figure 7

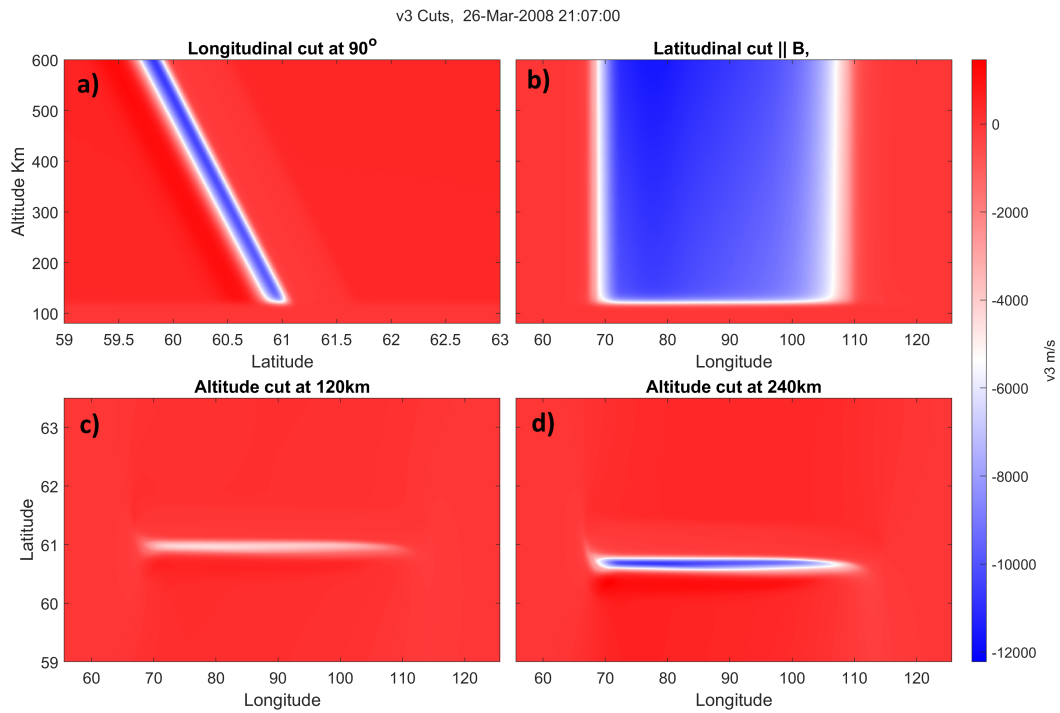


Figure 10. Channel east-west velocity at 07:00. All locations in latitude, longitude and altitude are the same as the ones shown on Figure 7

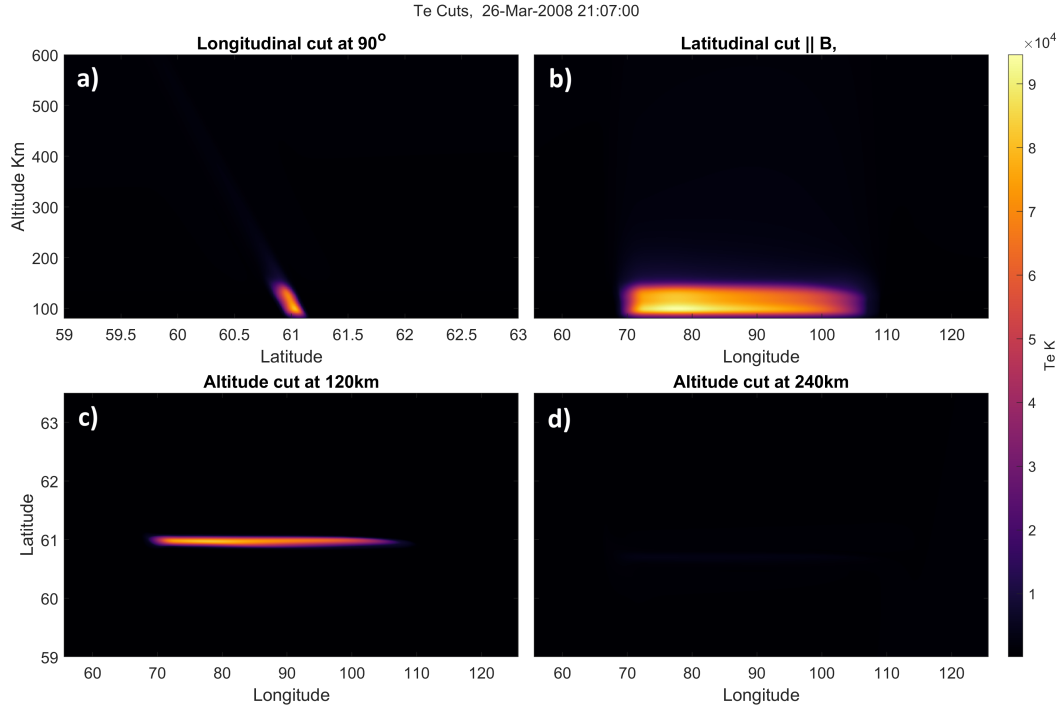


Figure 11. Electron temperature at 07:00. All locations in latitude, longitude and altitude are the same as the ones shown on Figure 7

573 In comparison, Figure 8a) and b) demonstrate how the F-region has begun to de-
 574plete, a phenomenon that is expected and also corroborated by DMSP measurements
 575(Nishimura, Donovan, et al., 2020). The extent of the depletion volume is now much larger
 576compared to Figure 7, and the eastern side once again exhibits its plasma depletion taper-
 577ing to lower altitudes. Figure 8c) further reveals that the eastern side of the plasma
 578depletion is narrower than at other longitudes. This can be explained by the fact that
 579in our 3D simulation, new plasma is being fed into the channel from the east at a constant
 580rate. This is a critical physical behavior that is missing from 2D simulations. From
 581Movie S1 and the previous snapshots, it is more appropriate to say that the growth is
 582damped rather than choked after the fact. Figure 8d) shows how the plasma depletion
 583at 240 km is of an order of magnitude, becoming wider as we move from the eastern edge
 584towards the west.

585 Indeed, by examining the channel velocity, we can appreciate the “travelling” of
 586its maximum value. Figure 9 and 10 display the east-west channel velocity at 03:00 and
 58707:00 minutes, respectively, with the panels representing the same locations as in Fig-
 588ure 7. By comparing the results on panel b) in both Figure 9 and 10, it becomes clear
 589that the maximum velocity starts on the eastern side and ends on the western side. This
 590is an expected result since the eastern side of the grid has had more time for the plasma
 591to recombine, thus having lower densities than the western side and reaching a larger plasma
 592depletion first. Later on, the western side catches up, and the velocity maximum shifts
 593to the western side. The width of the channel is approximately 0.5° degrees in latitude,
 594though its size is not perfectly uniform in longitude. This channel width agrees with the
 595measurements presented by Nishimura, Donovan, et al. (2020).

596 Finally, we should pay attention to the extreme electron temperatures that the sim-
 597ulation predicts between 100 and 150km. Figure 11 shows the electron temperature at
 59807:00 minutes in the same panel configuration as previous figures. This enhanced elec-
 599

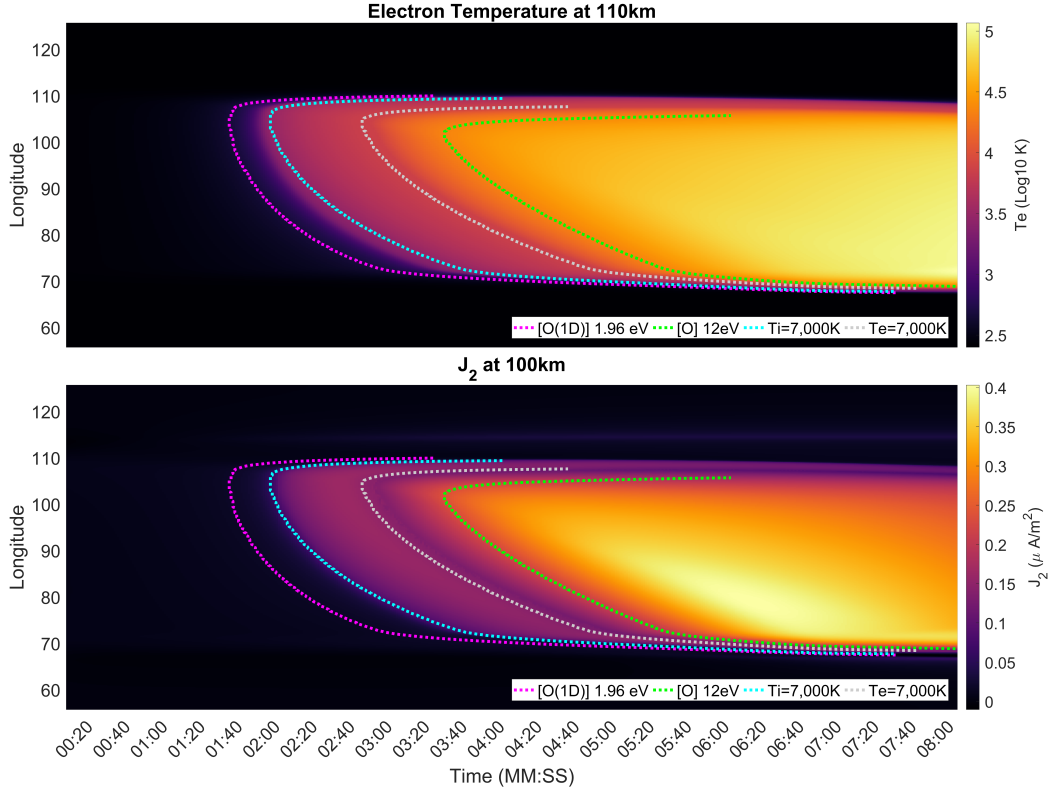


Figure 12. Electron temperature in logarithmic scale (top panel) and closure current at 100km (bottom panel). Y axis represents longitude at the center of the channel. Simulation starts when the 90° longitude point reaches 21 MLT

599 tron temperature happens in the same area where the plasma is extremely depleted, mak-
 600 ing the definition of temperature itself somewhat complicated. As previously stated, above
 601 7,000K the electron-neutral collisions grow unbound a linearly with temperature, and
 602 the positive feedback that exist on the frictional heating term makes the electron tem-
 603 perature grow unbound as well.

604 This also has an effect on the current density at lower altitudes. As shown in Fig-
 605 ure 2, current density is flowing at 100 km altitude, and this current is caused by the in-
 606 terplay between the enhancement in temperature causing larger collision frequencies, large
 607 enough that the collision frequency matches, and even surpasses, the electron cyclotron
 608 frequency, thus making the electrons collide in a small band. Figure 12 shows how the
 609 electron temperature and the closure current density change in time and longitude at
 610 110 km and 100 km respectively. Lines are also included to show the different thresh-
 611 olds defined previously. The increase in electron temperature on Figure 12(top) does fol-
 612 low the same behavior of starting in the east, with its maximum value traveling towards
 613 the west as time moves on. It also closely follows how the channel velocity behaves as
 614 seen on Figure 5(top), and therefore it is following the electric field caused by the driv-
 615 ing current density. This confirms the fact that our uncapped collision frequencies are
 616 indeed the culprit for the enhanced electron temperature. Figure 12(bottom) shows how
 617 the closure current density at 100 km has almost the same behavior as the channel ac-
 618 celeration, with it growing and decaying in a peak-valley-peak configuration also seen
 619 in Figure 5(bottom).

620

3.2 Comparison to 2D simulation

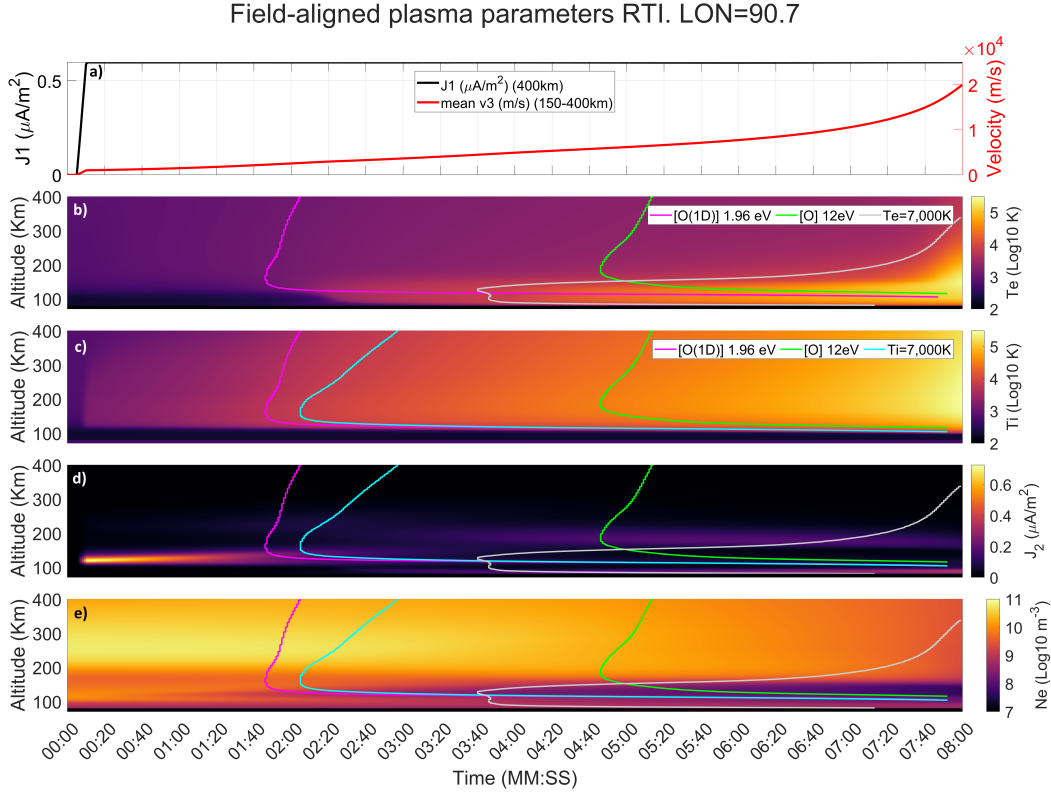


Figure 13. Field-aligned profiles are taken at the center of the flow channel for a 2D simulation. Panel a) displays values for parallel-to-B current density (J_1) and east/west velocity (v_3) at averaged from 150 to 400 km. Panels b) and c) showcase electron (T_e) and ion (T_i) temperatures, respectively. Panel d) depicts the north/south current (J_2), while panel e) provides insights into the total electron density (N_e)

As previously mentioned, there have been attempts to simulate an extreme SAID channel in 2D. Specifically, Liang et al. (2021) simulated an extreme SAID in 2D with a focus on potential generation, while in a subsequent paper, Liang et al. (2022) employed a current generation method. To directly compare 2D and 3D simulations, we established a GEMINI framework in 2D. The longitudinal coordinate was reduced to a single cell, and the driving current was adapted to match the pattern shown in panel a) of Figure 2.1 and Equation 1, while maintaining the same grid size and other input parameters. Supporting material for the 2D simulations can be seen on Figures S20 to S25 and Movies S18 to S21.

Figure 13 presents 2D simulation results, focusing on field-aligned profiles at the flow channel center, at the same location as Figure 2. Lines are also included to show the different thresholds defined previously. Similar to the 3D simulation, the companion Figure 14 specifically focuses on channel velocity, temperatures, specific ion densities, growth rates in velocity and temperature, as well as height-integrated conductivity. As before, the initial 5 seconds of the simulation do not have any current driver applied, with J_1 growing linearly during the subsequent 5 seconds to a value of approximately $0.6 \mu\text{A}/\text{m}^2$, remaining constant for the rest of the simulation, as shown in panel a) of Figure 13. The east/west velocity of the channel displayed in Figure 13 demonstrates

639 that the channel velocity reaches 1 km/s at 00:10, just like the 3D case. Figure 14a) and
 640 b) illustrate that there are some phases that can be divided into the peak-valley-peak
 641 configuration that the 3D simulations showed, though they are much more subdued and
 642 are only visible in the acceleration panel. The velocity appears to grow constantly, reach-
 643 ing an extreme value of 20 km/s by the end of the simulation, almost doubling its 3D
 644 counterpart at a maximum of 12 km/s.

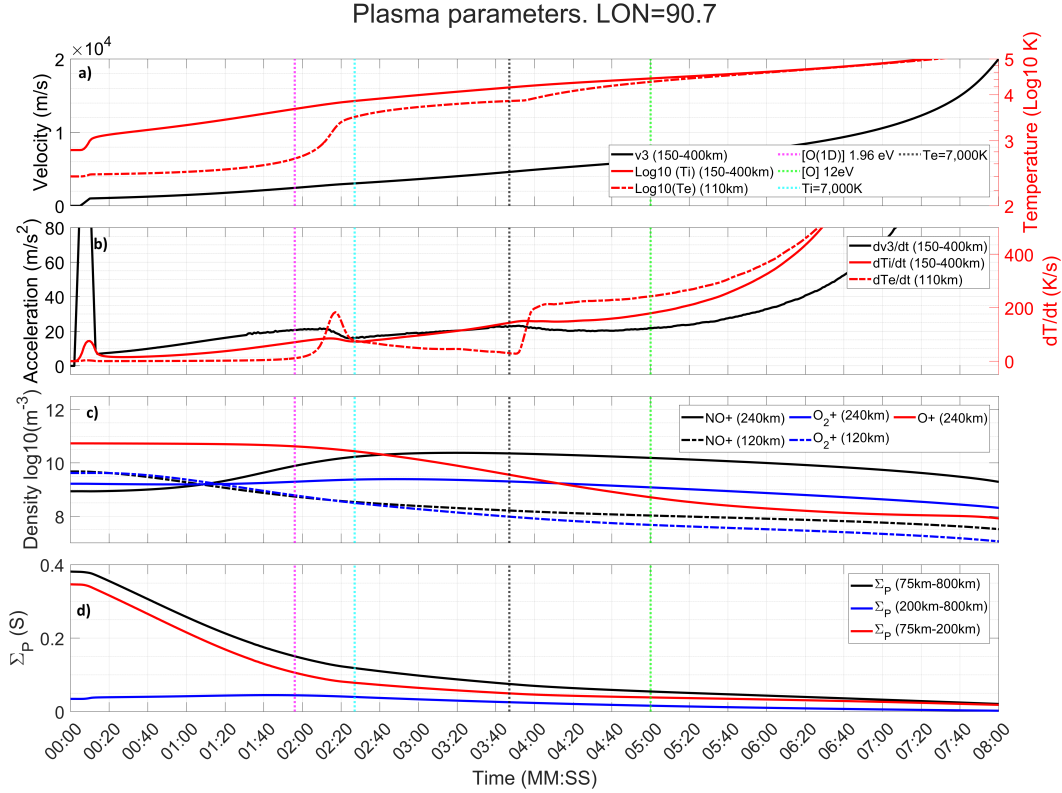


Figure 14. Miscellaneous output parameters of a 2D simulation. Panel a) shows the average channel velocity (v_3 , solid black line) and ion temperature (T_i , solid red line) between 150-400km, as well as the electron temperature (T_e , dashed red line) at 120km. Panel b) shows the time derivative of all variables shown on panel a). Panel c) shows the density of the main ions, $[NO^+]$ and $[O_2^+]$ at 120km (black and blue solid lines) and 240km (black and blue dashed lines) as well as $[O^+]$ at 240km (solid red line). Panel d) shows the total height integrated Pedersen conductance (Σ_p , solid black line), as well as the F-region (200-800km, solid blue line) and E-region (95-200km, solid red line) contribution

645 The first discernible phase begins at 00:10 minutes and ends approximately at 02:10
 646 minutes, as depicted in Figure 3a) and b), which aligns remarkably with the time frames
 647 of the 3D simulation. From Figure 13a), we observe that the channel velocity increases
 648 steadily during this time, reaching a value of 2.8 km/s by the end of the phase. The ve-
 649 locity at the center longitude in the 3D case is only 200 m/s larger, with the maximum
 650 value being 600 m/s larger and the minimum value being 500 m/s smaller. The max-
 651 imum acceleration value is 20 m/s², which is slightly smaller than the acceleration at the
 652 center longitude in the 3D case at 25 m/s², and more closely matches the western part
 653 of the flow channel. The closure current primarily flows through the 110 to 130km re-
 654 gion as seen in Figure 13d), and the plasma density depletion begins roughly at 00:20
 655 minutes according to Figure 13e), coinciding with the 3D results. From Figure 3c), we

656 see that the plasma density depletion in the E-region (120 km) is very similar to the 3D
 657 case, with the densities of $[NO^+]$ and $[O_2^+]$ dropping below 10^9 particles/m³ by the end
 658 of the phase. This is also reflected in the conductance in Figure 3d), where it reaches
 659 a value of 0.12 S, closely matching the 3D simulation. Once again, the end of the phase
 660 closely aligns with the point where $[NO^+]$ and $[O^+]$ are within an order of magnitude
 661 of each other at 240 km.

662 During this first phase, analogous to the 3D case, we have that $[O_2^+]$ reaches the
 663 threshold energy needed for the O(¹D) excitation state to happen at about 01:40. Which
 664 means that from that point on, energy will be lost to inelastic collisions, decreasing the
 665 channel velocity without affecting the electric field. Once again, this is the first impor-
 666 tant effects not included in GEMINI. The lower F-region also reaches temperatures above
 667 7,000K at approximately 02:00, with the average ion temperature between 150-400km
 668 reaching the same value later a 02:25, affecting the losses due to rotational and vibra-
 669 tions modes of $[N_2]$ and $[O_2]$.

670 The second phase spans from 02:10 minutes to 03:50, which is considerably longer
 671 than the 3D case. It exist roughly between the thresholds for the ion temperature and
 672 electron temperature reaching 7,000K. From Figure 13a), it is evident that the channel
 673 velocity and acceleration are no longer similar to those in the 3D case. The channel ve-
 674 locity steadily increases, reaching 4.8 km/s by the 03:50 minute mark, which is signif-
 675 icantly smaller than the 6.7 km/s shown by the 3D simulations at the same time. There
 676 are similarities in the behavior of the closure current density, with Figure 13d) illustrat-
 677 ing how the closure current begins to flow at 180 km and 100 km, much like the 3D case.
 678 Figure 13e) indicates that the depletion of plasma density in the E-region is very simi-
 679 lar in value to the 3D case during this time frame, although the depletion in the 3D case
 680 begins a few seconds earlier. From Figure 14a), we observe that the electron tempera-
 681 ture behaves in the same way as in the 3D case. From Figure 14b), it is apparent that
 682 even though the shape of the peak-valley-peak is somewhat preserved, the large differ-
 683 ences in the maximum values and time frames result in a channel that is very different
 684 in terms of velocity.

685 Finally, our last phase, which commences at 03:50 minutes and continues until the
 686 end of the simulation, illustrates how the differences from the 3D version become much
 687 more pronounced and extreme. It is important to remember though that after this point
 688 the electron-neutral collisions can grow unbound, thus affecting the results by allowing
 689 the electron temperature to grow in the same manner.

690 As depicted in Figure 13a), the channel velocity consistently increases, reaching 14
 691 km/s by the end of the simulation. From Figure 13b) and c), both the ion and electron
 692 temperatures reach extreme values, at 220,000 K for ions and 150,000 K for electrons.
 693 The closure current primarily flows at 180 km and 100 km from 03:50 onwards, as seen
 694 in Figure 13d). Figure 14a) and b) convey the same narrative, with a constant increase
 695 in channel velocity, temperatures, acceleration, and temperature growth. Unlike the 3D
 696 simulation, there is no decrease in acceleration. Figure 14c) reveals some of the reasons
 697 for such a stark difference: the plasma densities of $[NO^+]$ and $[O_2^+]$ in the E and F-region
 698 never reach a steady state and constantly decrease over time, attaining lower values than
 699 in the 3D simulation.

700 The plasma density of $[O^+]$ exhibits the same trend, with a constant decrease in
 701 density which does reach a certain constant value, whereas the 3D version experienced
 702 an increase in it. These differences in plasma densities and temperatures significantly
 703 impact the height-integrated conductance, as it falls below the 3D case by the end of the
 704 simulation, as seen in panel d), with a final value of 0.018 S compared to 0.026 S for the
 705 3D case.

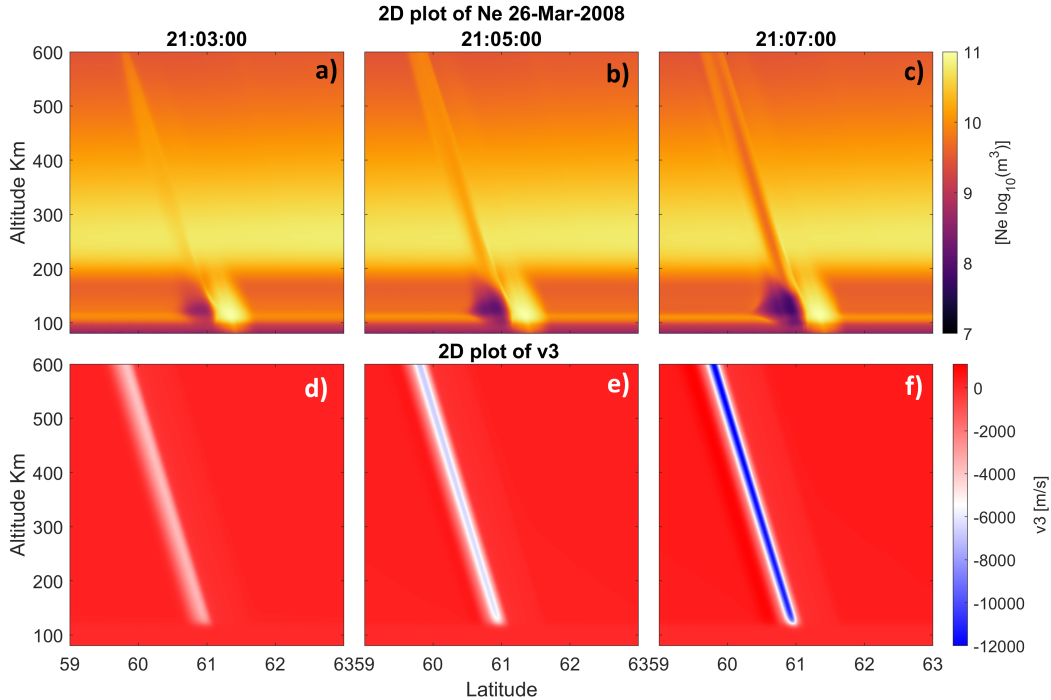


Figure 15. Total plasma density (top row) and channel velocity (bottom row) at 03:00 in panel a) and d), 05:00 in panel b) and e), and 07:00 in panel c) and f)

At the 05:00 minute mark the threshold for $[O_2^+]$ becoming 12eV is reached. It is expected then that plasma will start to be generated in E-region above 115km, affecting the conductance and thus limiting the maximum value of the channel velocity. In comparison to the 3D case, which had ionization from 120km upwards, the E-region will have more density generated, therefore a larger conductance and finally a larger decrease in the channel velocity.

Full 2D snapshots at 03:00, 05:00, and 07:00 are displayed in Figure 15. From panels a) through c), we can observe how the density depletion once again commences in the E-region. The primary differences between this and Figures 7 and 8 lie in the minimum values, with the 2D depletion being lower than the 3D, and the behavior of the channel in the F-region. From the 3D simulations, we obtain a dynamic shape in longitudes and varying channel widths, which influence the F-region portion of the channel. Since 2D lacks that additional coordinate, we can observe how the plasma depletion in the F-region is uniform in altitude and at a lower plasma density than its 3D counterpart. From panels d) through f), we can discern that the channel width is somewhat constant over time, at approximately 0.4° in latitude.

4 Discussion

This study presents a time-dependent 3D simulation of an extreme SAID channel, aiming to elucidate the emergence of the STEVE phenomena. Our focus lies in the lower F-region and the E-region, where direct experimental measurements are currently absent. Due to STEVE's wandering behavior, there exist few, if any, rocket or radar measurements, necessitating reliance on sparse satellite measurements between 400km (SWARM) and 850km (DMSF). From these measurements, we developed a 3D simulation driven solely by the current density on the grid's upper boundary. We made necessary mod-

730 ifications for the simulation to operate under the extreme conditions where the STEVE
 731 phenomena are presumed to exist and simulated the ionospheric changes due to such cur-
 732 rent density. We demonstrated the validity of the current generation method to create
 733 an SAID, as explained by Anderson et al. (1993) and their subsequent work. We estab-
 734 lished a direct relationship between the current density value and shape driving the sys-
 735 tem and the velocity of the generated SAID channel. Using the results of Nishimura, Dono-
 736 van, et al. (2020) as an initial reference, we drove the system with current densities ap-
 737 proaching over $0.6\mu\text{A}/\text{m}^2$.

738 We managed to produce flow velocities up to 12km/s, exceeding the 4.5km/s mea-
 739 sured by DMSP, and observed larger ion and electron temperatures than those measured.
 740 The increase in the channel velocity during its initial existence is primarily due to the
 741 decrease in conductance caused by the current density closing through the E-region, al-
 742 though this decrease is not unbounded. We showed that the entire F-region is not fully
 743 depleted as the simulation progresses. The densities of the main ions reach a steady state
 744 after a few minutes, maintaining the closure current at a higher altitude and entirely avoid-
 745 ing the E-region. Consequently, there is not a linear increase in velocity throughout the
 746 entire simulation, only while the E-region is being strongly depleted. The primary rea-
 747 son for this behavior is the suppressed growth in $E \times B$ drift on the eastern side, here
 748 new plasma is introduced into the channel. On the eastern side, plasma sources and a
 749 clockwise velocity vortex pinch the channel, reducing its longitudinal length and prevent-
 750 ing the plasma density from depleting.

751 Our simulations provide insight into how the driving factors affect an extreme SAID
 752 flow channel. Starting with the current density, a larger value leads to a larger steady-
 753 state channel velocity. A larger current density implies a larger electric field for a con-
 754 stant conductivity. However, this is not the only factor that influences the behavior of
 755 the channel velocity. The longitudinal length also has a direct relationship with it, with
 756 a longer channel in longitude producing larger velocities. Our raised cosine shape for the
 757 longitudinal characteristics of the current density enabled us to alter the length in lon-
 758 gitude at which the driving current is at its maximum value. Consequently, the longer
 759 the current is at its maximum, the greater the channel velocity. We conducted some sim-
 760 ulations with the inclusion of a blanket background precipitation. This did not elimi-
 761 nate the channel but rather extended the time frames at which events occur and marginally
 762 limited the flow channel velocity. The final modification to the driving factors was the
 763 width of the channel in latitude, with a wider channel exhibiting larger velocities for the
 764 same current density. However, this is not entirely realistic, as we expect that in a wider
 765 channel, the current density will be much smaller and fall into the SAPS category.

766 We also showed in detail how are simulations are lacking inelastic collisions and im-
 767 pact ionization, and how the threshold for these two events (1.96eV for $\text{O}(^1\text{D})$ excita-
 768 tion state and 12eV for $[\text{O}]$ ionization) happens in time and space. Both this threshold
 769 will provide means for slowing the channels velocity growth, thus the 12km/s final ve-
 770 locity must be considered more of a reference than a real channel velocity. Threshold for
 771 temperatures going above what the current equations boundaries are where also included,
 772 and allowed us to see why the phases happen they way they do.

773 The decision not to cap the electron temperature when calculating collision frequen-
 774 cies between electrons and neutrals that positively depend on the electron temperature
 775 is nuanced. Both approaches exist outside of any measured or theorized physics, render-
 776 ing them both flawed. We chose to leave these temperatures uncapped since our results
 777 would exist outside the current understanding of the collision processes occurring in the
 778 E-region, regardless of the approach. The only temperatures capped were those that neg-
 779 atively depend on the electron temperature, as these would generate negative collision
 780 frequencies and cause the model to error out upon reaching such temperatures. As a di-
 781 rect consequence of this decision, we have current flowing at 100 km, where the collision
 782 frequency between electrons and neutrals (particularly molecular oxygen) becomes higher

783 than the local electron cyclotron frequency. This implies that the electric field necessary
 784 to drive the closure current density to flow northward is smaller than if we had decided
 785 to cap the temperatures. If the enhancement of Pedersen conductivity at 100 km does
 786 not exist, the current density still needs to close through the sparse E-region plasma avail-
 787 able and the lower F-region plasma. This, in turn, means that the electric field would
 788 need to be even larger to allow for more current to flow under such a change in Peder-
 789 sen conductivity, resulting in a faster channel velocity, larger energies for $[NO^+]$ and $[O_2^+]$,
 790 and pushing the simulation even further from our known physics formulas of tempera-
 791 ture, collision frequencies, and transport.

792 Lynch et al. (2022) and Liang et al. (2021) both utilized an electric field driver, which
 793 allowed the current density to adjust itself to whatever is needed for such driving poten-
 794 tial. We argue that the current-driver is a better representation of M-I coupling, allow-
 795 ing the electric field to adjust itself to a value that allows such a current density to ex-
 796 ist. Even this assumptions has it drawbacks, as the conditions and details of where cur-
 797 rent is closing under these extreme conditions is not well known. At the same time, a
 798 constant current density at the top of the grid might not be the best approximation, as
 799 current variations are known to exist and are related to the ring current itself. As such
 800 our model predictions will require validation from further measurements of campaigns.

801 4.1 Role of 3D over 2D simulations

802 We have also conducted 2D simulations using the same driving factors as their 3D
 803 counterparts. From these, we learned that during the initial time frames, the channels
 804 behave similarly between 2D and 3D, with the main phases of the channel existing present.
 805 However, the differences become stark thereafter. In the absence of the longitudinal co-
 806 ordinate, the channel grows without bounds, with the plasma density being depleted at
 807 all altitudes. Thus, the conductance reaches incredibly low values and is constantly de-
 808 creasing, unlike in the 3D simulation. The 3D simulation of the extreme SAID flow chan-
 809 nel has provided numerous insights into the complex dynamics of this phenomenon. The
 810 results have revealed intricate structures and behaviors that are inherently three-dimensional,
 811 underscoring the importance of using 3D simulations for such studies. This added com-
 812 plexity can yield more accurate and realistic results. However, it also introduces more
 813 complexity into the simulation and the subsequent analysis of the results.

814 Choosing between 2D and 3D simulations involves trade-offs. One of the main con-
 815 siderations is that 3D simulations require significantly more computational resources than
 816 2D simulations. They involve more data points, leading to increased memory require-
 817 ments, and more computations per time step, which escalates the processing power and
 818 time needed. This can be a limiting factor, particularly for complex systems or simula-
 819 tions that span long periods.

820 While 2D simulations can offer valuable insights and are often employed for ini-
 821 tial explorations, they may not fully encapsulate the behavior of systems that are inher-
 822 ently 3D, leading to a loss of information due to the collapse of one dimension. In such
 823 instances, 3D simulations can provide a more accurate representation. However, visu-
 824 alizing and interpreting the results of 3D simulations can be more challenging than for
 825 2D simulations due to the additional dimension and the constraints of 2D plots. On the
 826 other hand, this simplification can distort the representation of the system, especially
 827 when the collapsed dimension contains critical information. 3D simulations retain all spa-
 828 tial information, offering a more comprehensive and accurate depiction of the system.
 829 One of the most striking findings from the 3D simulation is the presence of significant
 830 structure in the longitudinal coordinate, which is not captured in 2D simulations. This
 831 structure has a profound impact on the behavior of the SAID channel, specifically the
 832 plasma sources and flows that seem to constrain the channel growth in the east. These
 833 structures play a pivotal role in shaping the dynamics of the SAID channel, influencing

its velocity and temperature. Since 2D lacks the new plasma coming into the channel from the longitudinal direction, the plasma depletion is unbounded and reaches values much lower than its 3D counterpart. This is especially important in the F-region, where most of the current flows after the E-region is completely depleted. This in part allows the conductance to decrease to very small values which, in turn, increases the electric field in order to maintain a constant current through the system.

4.2 On the need for future improvements to modeling

While this study has addressed 3D structure of flow channels, the simulations presented herein should be interpreted as approximate in only a very rough sense for a number of reasons. Foremost there are relatively few observations that allow us to constrain the model inputs so it is not clear whether we are simulating a somewhat typical STEVE event or one of the most extreme events ever observed. It should also be noted that a number of assumptions needed to be made in order to even achieve sensible results in our model – some of which could impact the ionospheric behavior substantially. These largely concern parameterizations of collisional processes (cf. Section 2.2) which apparently become invalid at the energies required for our analysis. We have chosen to calculate these collisional processes using a temperature with a set ceiling; however, a more physically-motivated extrapolation would be preferable for future studies in such extreme conditions. Finally, ion energies that result from our modeling are well above the limits that would trigger inelastic ion-neutral and ion-ion collisions – these are not included presently (it is not clear whether the requisite cross-section data are even available) but likely represent an important energy sink that will limit temperatures.

5 Summary and future work

The presented study demonstrates our ability to simulate an extreme SAID channel, with results surpassing the current measurements of STEVE. The simulations unveiled intricate structures and behaviors, underscoring the significance of 3D simulations in capturing these phenomena. The correlation between plasma depletion, conductance increase, and channel velocity increase is validated, even at the extreme velocities of 12km/s. The research also highlights the influence of various factors, such as current density and longitudinal length, on the behavior of the channel velocity. However, these simulations should be considered as approximations due to the scarcity of observations available to constrain the model inputs and the assumptions made to obtain plausible results. Simulation results produce features that are qualitative consistent with optical and space-based observations, while exposing the physical limitations of current models used in SAID-STEVE studies. We show that a plausible ionosphere created by driving it with measured STEVE drivers rapidly reaches parameter values that are beyond the limits of applicability of the governing equations, and beyond known physical limits of the key collisional models used. In particular, effects of inelastic collisions and impact ionization will likely become an important consideration in STEVE.

We pushed GEMINI to the boundaries of what is stable, as well as made assumptions about collisional terms that might affect the final results. The way the simulation was set up leaves us with many important points that must be remembered:

- A 3D grid was utilized that followed a tilted dipole coordinate system. This grid spans from 0 to 100km in altitude, 58° to 64° in latitude, and 55° to 125° in longitude. The grid size was set at 512x512x512.
- The simulation was driven by a field-aligned current density shape as seen on Figure 2.1. The shape in latitude was chosen as two opposite sign Gaussian's, which allowed us to have and up and down current density with smooth edges, something essential for modelling. Precipitating electrons were added on the upward por-

883 tion of the current, to simulate a current carried by precipitating electrons. In lon-
 884 gitude, a raised-cosine shape was used so that we could have a long and constant
 885 longitudinal shape, yet a smooth transition to zero at the edges.

- 886 • A maximum value of $0.6\mu\text{A}/\text{m}^2$ for the driving current density was chosen. This
 887 agrees with previous measurements, though smaller than what Nishimura, Dono-
 888 van, et al. (2020) measures.
- 889 • GEMINI underwent changes to some of its internal code in order to accommodate
 890 the extreme velocities and temperatures. Particularly some electron-neutral col-
 891 lision frequencies had to be capped since at higher temperatures they would be-
 892 come negative.
- 893 • GEMINI numerical solver was also adapted to solve its thermal conductivity and
 894 source-loss terms simultaneously to avoid oscillations due to the high temperatures.
- 895 • Since there are no inelastic collisions nor impact ionization terms in GEMINI, one
 896 must consider our results as a reference, in reality these and other kinetic processes
 897 are expected to be triggered at these extremes situations.

898 Our results show how there are distinct phases in time during the creation and ex-
 899 istence of an extreme SAID channel, as well as how the phases might be related to the
 900 different plasma densities and transport inside the extreme SAID channel. The lon-
 901 gitudinal aspect is critical, since the more eastward we are the channel grows faster, while
 902 the westward section grows slower but reaches much larger values of velocity and tem-
 903 perature. From our simulations, we can create a list of important results that need to
 904 be highlighted:

- 905 • The channel velocity grows exponentially, finishing with a linear growth, to val-
 906 ues of $12\text{km}/\text{s}$ on the western edge. This values are larger than the ones previously
 907 presented by Nishimura, Donovan, et al. (2020), and show how under a current
 908 smaller than measured it is possible to obtain extremely large flows. The real value
 909 will be smaller than this though, due to the omission of inelastic collisions nor im-
 910 pact ionization terms that will work against channel velocity growth.
- 911 • Approximately four phases exist during the 8 minute simulation time, not con-
 912 sidering the initial 10 second where the driving current density grows fast to its
 913 maximum value.
- 914 • The first phase can be described as an exponential growth in velocity up to $1\text{km}/\text{s}$,
 915 most of the closure current flows through the 110 to 130km region and the E-region
 916 is rapidly being depleted. From a few second in, there is enough ion temperature
 917 to trigger the most important reaction: $[O^+] + [N_2] \rightarrow [NO^+] + [N]$ which de-
 918 pletes the $[O^+]$ in the lower F region. During this phase inelastic collisions will
 919 start to happen, thus decreasing the velocity due to energy being soaked up.
- 920 • A second phase happens between two local maxima of the acceleration of the chan-
 921 nel, roughly existing between the points where the ion and electron temperature
 922 reach $7,000\text{K}$. During this time $[O^+]$ is being rapidly depleted in the F region, while
 923 the E-region densities continue their exponential decrease. This section is char-
 924 acterised by a large growth in the acceleration, as well as electron temperature.
 925 During this phase we still have valid electron-neutral collision frequencies. The
 926 second phase is also characterised by the closure current flowing through other al-
 927 titudes rather than the 110 to 130km region.
- 928 • Our third phase only exist on the westward portion of the channel, with its end
 929 coinciding with the point where the density of $[O^+]$ in the F-region reaches the
 930 values of the density of plasma in the E-region. It has the largest acceleration com-
 931 pared to other phases. At this point, we have a total $400\text{mV}/\text{m}^2$ electric field. The
 932 electron temperature is now larger than $7,000\text{K}$, thus the collision frequencies grow
 933 unbound, affecting the frictional heating. During this phase $[O_2^+]$ reaches 12eV ,
 934 enough energy to ionize the ambient $[O]$, creating plasma from 120km upward and
 935 thus increasing the conductance, reducing the channel velocity in turn.

936 • The final phase exist on all locations in terms of longitude, and it is characterized
 937 by a constant and linear growth of the channel velocity, with a smaller slope than
 938 any other previous phase, confirmed by the much lower and constant acceleration.
 939 Densities of $[NO^+]$ and $[O_2^+]$ in the F-region reach a steady state where they re-
 940 main mostly constant. There is a slow increase of $[O^+]$ in the F-region. We are
 941 outside the boundaries of most validity for most equations at this point.

942 From these phases and the behaviour of the channel in both latitude and longitude,
 943 several important points can be made about how our simulation attempts to model the
 944 behavior of STEVE through an extreme SAID flow channel. From this, we can create
 945 a list of key takeaways from the simulations:

- 946 • This study has utilized 3D simulations to explore the dynamics of extreme SAID
 947 flow channels, with a focus on the STEVE phenomena.
- 948 • The simulations have revealed complex structures and behaviors, emphasizing the
 949 importance of 3D over 2D simulations in capturing these phenomena.
- 950 • Under a constant current density driver, the channel growth in velocity is not uni-
 951 form. Fast velocities are reaches in the eastern side first since it has less plasma
 952 to deplete due to plasma recombination. Western side grows slower due to the larger
 953 plasma in that region, but reaches velocities up to 10% higher than its opposite
 954 side.
- 955 • We predict testable changes in the ionosphere-thermosphere-magnetosphere sys-
 956 tem response when the temperature exceeds the turn-on threshold for the $[O^+]$
 957 + $[N_2]$ reaction.
- 958 • Chemistry in the E-region and lower F-region controls the channel velocity behav-
 959 ior. Once the E-region becomes almost completely depleted, current flows through
 960 the lower F-region.
- 961 • The omission of inelastic terms helps the channel to grow even more than what
 962 it would in real life. Same can be said about the impact ionization effect on the
 963 conductance.
- 964 • Temperature threshold are very important. In our case, since we left the collision
 965 frequencies between electrons and some neutrals uncapped if they would not reach
 966 negative values, we have an abnormal electron temperature increase in the E-region.
 967 It does not expand to higher altitudes since it depends mostly on the density of
 968 $[O_2]$. This causes the electron-neutral collision frequency to rise above the elec-
 969 tron cyclotron frequency in a small band at 100km, allowing current to flow there.
 970 If the collision frequencies were capped, we expect the electric field to adjust it-
 971 self to close the full amount of the current density through the lower F-region, re-
 972 sulting in an even faster flow channel.

973 5.1 Future work

974 We have demonstrated a 3D simulation of an extreme SAID channel in GEMINI,
 975 although several constraints were necessary for the model to operate within its limits.
 976 It is crucial to revisit the formulas and theories of collision frequencies/collision cross-
 977 sections of various ion-neutral and electron-neutral interactions. In this study, only the
 978 collision frequencies that would result in a negative number had their temperature capped
 979 at a maximum value, while others were left unbounded. The decision to cap or not cap
 980 the temperature in all calculations is complex, as both approaches make strong assump-
 981 tions on what is happening in the ionosphere.

982 The Geospace Dynamics Constellation (GDC) is a mission concept designed to study
 983 the coupling between the magnetosphere and the ionosphere/thermosphere system, which
 984 would include plasma drift sensors and more. The results that can be obtained by mod-
 985 eling the ionospheric behavior under an extreme electric field will be useful when search-

ing for signatures of STEVE in GDC data. Conversely, the presence of a sub-auroral phased array incoherent scatter radar, such as AMISR, for example, would provide the necessary data at lower altitudes to further understand the process of STEVE. This study allows us to conduct numerical experiments useful for the design of new instruments and networks. In conclusion, our simulations provide a detailed heterogeneous parameter set for comparison with current and future observations, including:

- ISR (Ne, T_e , T_i , ion composition)
- Imaging spectroscopy (ion abundances, electron energy/temperature)
- LEO satellites (GDC, DMSP, SWARM; temperatures, abundances, flows, precipitation)
- Multi-point observations (GDC constellations, camera networks)

Finally, the current simulations do not account for any effects caused by instabilities in the E and F-region. Due to the large electric field, we anticipate that the Farley-Buneman instability will occur between 100 and 120 km, leading to an increase in the electron temperature and a change in the conductivities. Liang et al. (2021) and Liang et al. (2022) incorporated the effects on the electron temperature in their 2D simulations, utilizing the theory developed by St-Maurice and Goodwin (2021). We plan to include the effects of the Farley-Buneman instability in a simulation of an extreme SAID channel using the results of Dimant and Oppenheim (2011a) and Dimant and Oppenheim (2011b) in the near future.

6 Open Research

The modified version of GEMINI, as well as the modified python code necessary to run it, is available in Zenodo: 10.5281/zenodo.10783352. Config files, including implementation functions for the current density and precipitation are also available in Zenodo: 10.5281/zenodo.10783372. Finally, the GEMINI model is being constantly improved and updated at <https://github.com/gemini3d>

Acknowledgments

JMDP was supported by NASA grant 80NSSC20K1356. MZ was supported by NASA grant 80NSSC21K1354. The work of YN was supported by NASA grants 80NSSC21K1321, 80NSSC22K0749, 80NSSC23M0193 and 80NSSC23K0410, NSF grants AGS-1907698 and AGS-2100975, AFOSR grants FA9550-23-1-0614 and FA9550-23-1-0634, and ISSI Bern/ISSJ-BJ for the "Multi-Scale Magnetosphere-Ionosphere-Thermosphere Interaction" and "Auroral Research Coordination: Towards Internationalised Citizen Science (ARCTICS)" teams.

References

- Anderson, P., Carpenter, D., Tsuruda, K., Mukai, T., & Rich, F. (2001). Multi-satellite observations of rapid subauroral ion drifts (said). *Journal of Geophysical Research: Space Physics*, *106*(A12), 29585–29599.
- Anderson, P., Hanson, W., Heelis, R., Craven, J., Baker, D., & Frank, L. (1993). A proposed production model of rapid subauroral ion drifts and their relationship to substorm evolution. *Journal of Geophysical Research: Space Physics*, *98*(A4), 6069–6078.
- Anderson, P., Heelis, R., & Hanson, W. (1991). The ionospheric signatures of rapid subauroral ion drifts. *Journal of Geophysical Research: Space Physics*, *96*(A4), 5785–5792.
- Archer, W., St.-Maurice, J.-P., Gallardo-Lacourt, B., Perry, G., Cully, C., Donovan,

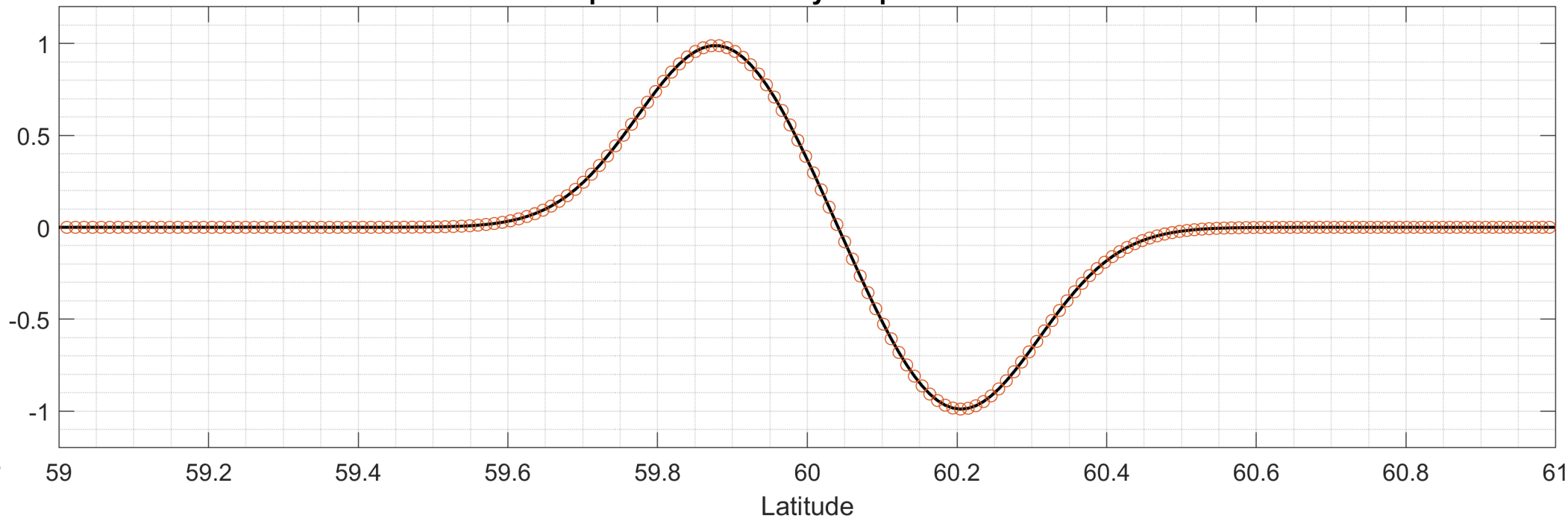
- 1032 E., ... Eurich, D. (2019). The vertical distribution of the optical emissions of
 1033 a steve and picket fence event. *Geophysical Research Letters*, *46*(19), 10719–
 1034 10725.
- 1035 Archer, W. E., Gallardo-Lacourt, B., Perry, G. W., St.-Maurice, J.-P., Buchert,
 1036 S. C., & Donovan, E. (2019). Steve: The optical signature of intense subauroral
 1037 ion drifts. *Geophysical Research Letters*, *46*(12), 6279–6286.
- 1038 Archer, W. E., & Knudsen, D. J. (2018). Distinguishing subauroral ion drifts from
 1039 birkeland current boundary flows. *Journal of Geophysical Research: Space
 1040 Physics*, *123*(1), 819–826.
- 1041 Banks, P. (1966). *Charged particle temperatures and electron thermal conductivity in
 1042 the upper atmosphere scientific report no. 276* (Tech. Rep. No. No. NASA-CR-
 1043 78936).
- 1044 Bilitza, D., Pezzopane, M., Truhlik, V., Altadill, D., Reinisch, B. W., & Pignal-
 1045 beri, A. (2022). The international reference ionosphere model: A review
 1046 and description of an ionospheric benchmark. *Reviews of Geophysics*, *60*(4),
 1047 e2022RG000792.
- 1048 Blelly, P., & Schunk, R. (1993). A comparative study of the time-dependent stan-
 1049 dard 8-, 13- and 16-moment transport formulations of the polar wind. *AnGeo*,
 1050 *11*(6), 443–469.
- 1051 De Keyser, J. (1999). Formation and evolution of subauroral ion drifts in the course
 1052 of a substorm. *Journal of Geophysical Research: Space Physics*, *104*(A6),
 1053 12339–12349.
- 1054 Dimant, Y., & Oppenheim, M. (2011a). Magnetosphere-ionosphere coupling through
 1055 e region turbulence: 1. energy budget. *Journal of Geophysical Research: Space
 1056 Physics*, *116*(A9).
- 1057 Dimant, Y., & Oppenheim, M. (2011b). Magnetosphere-ionosphere coupling through
 1058 e region turbulence: 2. anomalous conductivities and frictional heating. *Jour-
 1059 nal of Geophysical Research: Space Physics*, *116*(A9).
- 1060 Emmert, J. T., Drob, D. P., Picone, J. M., Siskind, D. E., Jones Jr, M., Mlynczak,
 1061 M., ... others (2021). Nrlmsis 2.0: A whole-atmosphere empirical model of
 1062 temperature and neutral species densities. *Earth and Space Science*, *8*(3),
 1063 e2020EA001321.
- 1064 Foster, J., Buonsanto, M., Mendillo, M., Nottingham, D., Rich, F., & Denig, W.
 1065 (1994). Coordinated stable auroral red arc observations: Relationship to
 1066 plasma convection. *Journal of Geophysical Research: Space Physics*, *99*(A6),
 1067 11429–11439.
- 1068 Foster, J., & Burke, W. (2002). Saps: A new categorization for sub-auroral electric
 1069 fields. *Eos, Transactions American Geophysical Union*, *83*(36), 393–394.
- 1070 Gallardo-Lacourt, B., Liang, J., Nishimura, Y., & Donovan, E. (2018). On the origin
 1071 of steve: Particle precipitation or ionospheric skyglow? *Geophysical Research
 1072 Letters*, *45*(16), 7968–7973.
- 1073 Gallardo-Lacourt, B., Nishimura, Y., Donovan, E., Gillies, D., Perry, G., Archer,
 1074 W., ... Spanswick, E. (2018). A statistical analysis of steve. *Journal of
 1075 Geophysical Research: Space Physics*, *123*(11), 9893–9905.
- 1076 Galperin, Y. I., & A.G., Z. (1974). Plasma convection in polar ionosphere. *Ann.
 1077 Geophys*, *30*(1).
- 1078 Gillies, D. M., Donovan, E., Hampton, D., Liang, J., Connors, M., Nishimura, Y., ...
 1079 Spanswick, E. (2019). First observations from the trex spectrograph: The opti-
 1080 cal spectrum of steve and the picket fence phenomena. *Geophysical Research
 1081 Letters*, *46*(13), 7207–7213.
- 1082 Gillies, D. M., Liang, J., Gallardo-Lacourt, B., & Donovan, E. (2023). New in-
 1083 sight into the transition from a sar arc to steve. *Geophysical Research Letters*,
 1084 *50*(6), e2022GL101205.
- 1085 Harding, B. J., Mende, S. B., Triplett, C. C., & Wu, Y.-J. J. (2020). A mecha-
 1086 nism for the steve continuum emission. *Geophysical Research Letters*, *47*(7),

- e2020GL087102.
- 1087 Huba, J., Joyce, G., & Fedder, J. (2000). Sami2 is another model of the iono-
 1088 sphere (sami2): A new low-latitude ionosphere model. *Journal of Geophysical*
 1089 *Research: Space Physics*, *105*(A10), 23035–23053.
- 1090 Huba, J., Joyce, G., & Krall, J. (2008). Three-dimensional equatorial spread f mod-
 1091 eling. *Geophysical Research Letters*, *35*(10).
- 1092 Itikawa, Y. (1974). Momentum-transfer cross sections for electron collisions with
 1093 atoms and molecules. *Atomic data and nuclear data tables*, *14*(1), 1–10.
- 1094 Jones, D. B., Campbell, L., Bottema, M., & Brunger, M. J. (2003). New electron-
 1095 energy transfer rates for vibrational excitation of o2. *New Journal of Physics*,
 1096 *5*(1), 114.
- 1097 LeVeque, R. J. (2007). *Finite difference methods for ordinary and partial differential*
 1098 *equations: steady-state and time-dependent problems*. SIAM.
- 1099 Liang, J., Donovan, E., Connors, M., Gillies, D., St-Maurice, J., Jackel, B., ... Chu,
 1100 X. (2019). Optical spectra and emission altitudes of double-layer steve: A case
 1101 study. *Geophysical Research Letters*, *46*(23), 13630–13639.
- 1102 Liang, J., St-Maurice, J., & Donovan, E. (2021). A time-dependent two-dimensional
 1103 model simulation of lower ionospheric variations under intense said. *Journal of*
 1104 *Geophysical Research: Space Physics*, *126*(12), e2021JA029756.
- 1105 Liang, J., St-Maurice, J.-P., & Donovan, E. (2022). Model simulation of said
 1106 intensification in the ionosphere under a current generator: the role of ion ped-
 1107 ersen transport. *Journal of Geophysical Research: Space Physics*, *127*(11),
 1108 e2022JA030960.
- 1109 Lynch, K. A., McManus, E., Gutow, J., Burleigh, M., & Zettergren, M. (2022).
 1110 An ionospheric conductance gradient driver for subauroral picket fence visible
 1111 signatures near steve events. *Journal of Geophysical Research: Space Physics*,
 1112 *127*(12), e2022JA030863.
- 1113 Lyons, L., Nishimura, Y., & Zou, Y. (2016). Unsolved problems: Mesoscale polar
 1114 cap flow channels' structure, propagation, and effects on space weather distur-
 1115 bances. *Journal of Geophysical Research: Space Physics*, *121*(4), 3347–3352.
- 1116 MacDonald, E. A., Donovan, E., Nishimura, Y., Case, N. A., Gillies, D. M.,
 1117 Gallardo-Lacourt, B., ... others (2018). New science in plain sight: Citizen
 1118 scientists lead to the discovery of optical structure in the upper atmosphere.
 1119 *Science advances*, *4*(3), eaaq0030.
- 1120 Martinis, C., Griffin, I., Gallardo-Lacourt, B., Wroten, J., Nishimura, Y., Baum-
 1121 gardner, J., & Knudsen, D. (2022). Rainbow of the night: First direct obser-
 1122 vation of a sar arc evolving into steve. *Geophysical Research Letters*, *49*(11),
 1123 e2022GL098511.
- 1124 Mishin, E., Nishimura, Y., & Foster, J. (2017). Saps/said revisited: A causal re-
 1125 lation to the substorm current wedge. *Journal of Geophysical Research: Space*
 1126 *Physics*, *122*(8), 8516–8535.
- 1127 Nishimura, Y., Deng, Y., Lyons, L. R., McGranaghan, R. M., & Zettergren, M. D.
 1128 (2021). Multiscale dynamics in the high-latitude ionosphere. *Ionosphere*
 1129 *dynamics and applications*, 49–65.
- 1130 Nishimura, Y., Donovan, E., Angelopoulos, V., & Nishitani, N. (2020). Dynamics
 1131 of auroral precipitation boundaries associated with steve and said. *Journal of*
 1132 *Geophysical Research: Space Physics*, *125*(8), e2020JA028067.
- 1133 Nishimura, Y., Gallardo-Lacourt, B., Zou, Y., Mishin, E., Knudsen, D., Donovan, E.,
 1134 ... Raybell, R. (2019). Magnetospheric signatures of steve: Implications for
 1135 the magnetospheric energy source and interhemispheric conjugacy. *Geophysical*
 1136 *Research Letters*, *46*(11), 5637–5644.
- 1137 Nishimura, Y., Yang, J., Weygand, J., Wang, W., Kosar, B., Donovan, E., ... Nishi-
 1138 tani, N. (2020). Magnetospheric conditions for steve and said: Particle in-
 1139 jection, substorm surge, and field-aligned currents. *Journal of Geophysical*
 1140 *Research: Space Physics*, *125*(8), e2020JA027782.
- 1141

- 1142 Ober, D. M., Horwitz, J., & Gallagher, D. (1997). Formation of density troughs
1143 embedded in the outer plasmasphere by subauroral ion drift events. *Journal of*
1144 *Geophysical Research: Space Physics*, *102*(A7), 14595–14602.
- 1145 Pavlov, A. (1998). New electron energy transfer rates for vibrational excitation of
1146 n₂. *Annales Geophysicae*, *16*(2), 176–182.
- 1147 Puhl-Quinn, P., Matsui, H., Mishin, E., Mouikis, C., Kistler, L., Khotyaintsev, Y.,
1148 ... Lucek, E. (2007). Cluster and dmsp observations of said electric fields.
1149 *Journal of Geophysical Research: Space Physics*, *112*(A5).
- 1150 Qian, L., Burns, A. G., Emery, B. A., Foster, B., Lu, G., Maute, A., ... Wang,
1151 W. (2014). The ncar tie-gcm: A community model of the coupled thermo-
1152 sphere/ionosphere system. *Modeling the ionosphere–thermosphere system*,
1153 73–83.
- 1154 Radicella, S. M. (2009). The nequick model genesis, uses and evolution. *Annals of*
1155 *geophysics*, *52*(3-4), 417–422.
- 1156 Ridley, A., Deng, Y., & Toth, G. (2006). The global ionosphere–thermosphere
1157 model. *Journal of Atmospheric and Solar-Terrestrial Physics*, *68*(8), 839–864.
- 1158 Schunk, R. (1977). Mathematical structure of transport equations for multispecies
1159 flows. *Reviews of Geophysics*, *15*(4), 429–445.
- 1160 Schunk, R., & Nagy, A. (2009). *Ionospheres: physics, plasma physics, and chemistry*.
1161 Cambridge university press.
- 1162 Semeter, J., Hunnekuhl, M., MacDonald, E., Hirsch, M., Zeller, N., Chernenkoff, A.,
1163 & Wang, J. (2020). The mysterious green streaks below steve. *AGU Advances*,
1164 *1*(4), e2020AV000183.
- 1165 Southwood, D., & Wolf, R. (1978). An assessment of the role of precipitation in
1166 magnetospheric convection. *Journal of Geophysical Research: Space Physics*,
1167 *83*(A11), 5227–5232.
- 1168 Spiro, R., Heelis, R., & Hanson, W. (1979). Rapid subauroral ion drifts observed by
1169 atmosphere explorer c. *Geophysical Research Letters*, *6*(8), 657–660.
- 1170 St-Maurice, J.-P., Cussenot, C., & Kofman, W. (1999). On the usefulness of e region
1171 electron temperatures and lower f region ion temperatures for the extraction of
1172 thermospheric parameters: a case study. In *Annales geophysicae* (Vol. 17, pp.
1173 1182–1198).
- 1174 St-Maurice, J.-P., & Goodwin, L. (2021). Revisiting the behavior of the e-region
1175 electron temperature during strong electric field events at high latitudes. *Jour-*
1176 *nal of Geophysical Research: Space Physics*, *126*(2), 2020JA028288.
- 1177 St-Maurice, J.-P., & Laneville, P. (1998). Reaction rate of o⁺ with o₂, n₂, and
1178 no under highly disturbed auroral conditions. *Journal of Geophysical Research:*
1179 *Space Physics*, *103*(A8), 17519–17521.
- 1180 Wright, A. N., & Russell, A. J. (2014). Alfvén wave boundary condition for re-
1181 sponsive magnetosphere-ionosphere coupling. *Journal of Geophysical Research:*
1182 *Space Physics*, *119*(5), 3996–4009.
- 1183 Zettergren, M., & Semeter, J. (2012). Ionospheric plasma transport and loss in auro-
1184 ral downward current regions. *Journal of Geophysical Research: Space Physics*,
1185 *117*(A6).
- 1186 Zettergren, M., Semeter, J., & Dahlgren, H. (2015). Dynamics of density cavities
1187 generated by frictional heating: Formation, distortion, and instability. *Geo-*
1188 *physical Research Letters*, *42*(23), 10–120.
- 1189 Zettergren, M., & Snively, J. (2019). Latitude and longitude dependence of iono-
1190 spheric tec and magnetic perturbations from infrasonic-acoustic waves gen-
1191 erated by strong seismic events. *Geophysical Research Letters*, *46*(3), 1132–
1192 1140.
- 1193 Zheng, Y., Brandt, P. C., Lui, A. T., & Fok, M.-C. (2008). On ionospheric trough
1194 conductance and subauroral polarization streams: Simulation results. *Journal*
1195 *of Geophysical Research: Space Physics*, *113*(A4).

Figure 1.

Input current density shape in Latitude



Input current density shape in Longitude

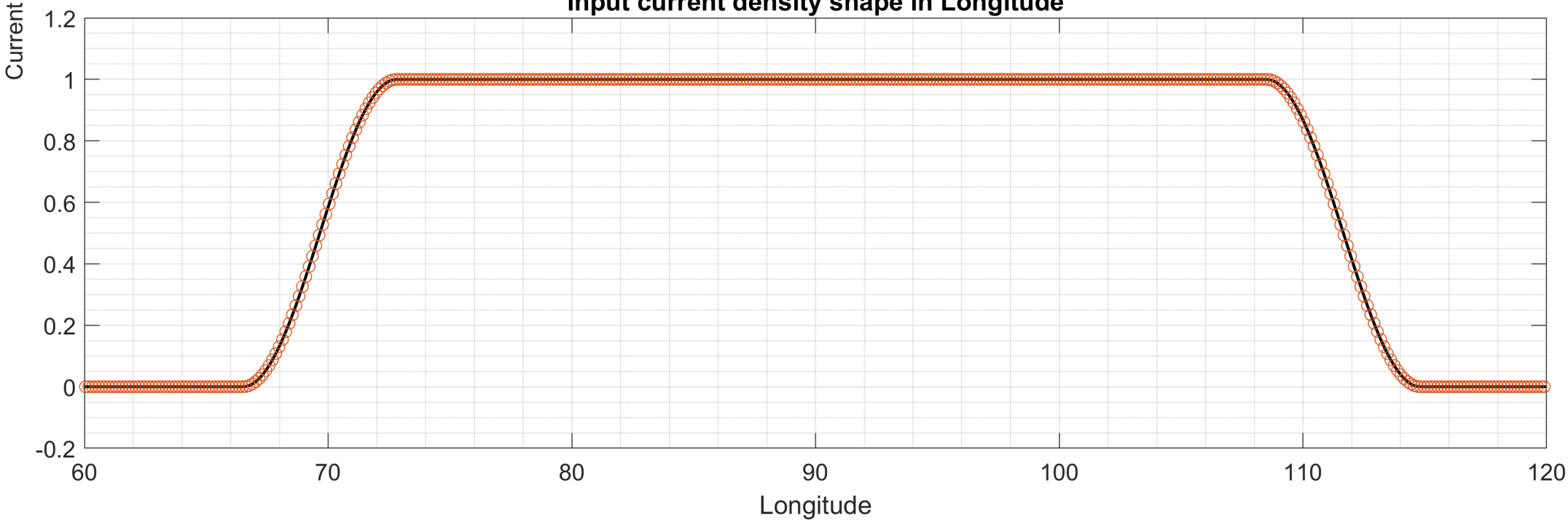


Figure 2.

Field-aligned plasma parameters RTI. LON=90.6

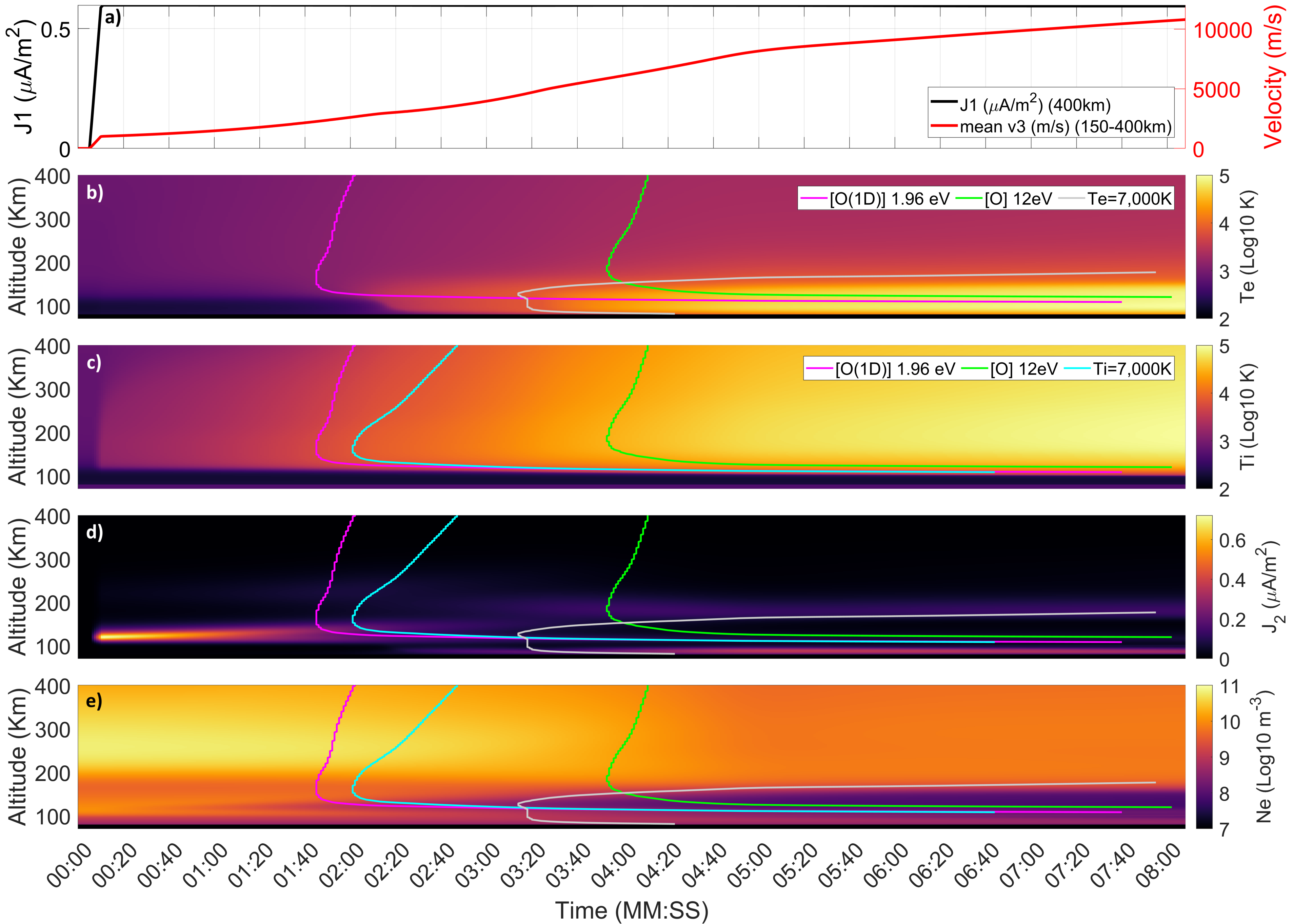


Figure 3.

Plasma parameters. LON=90.6

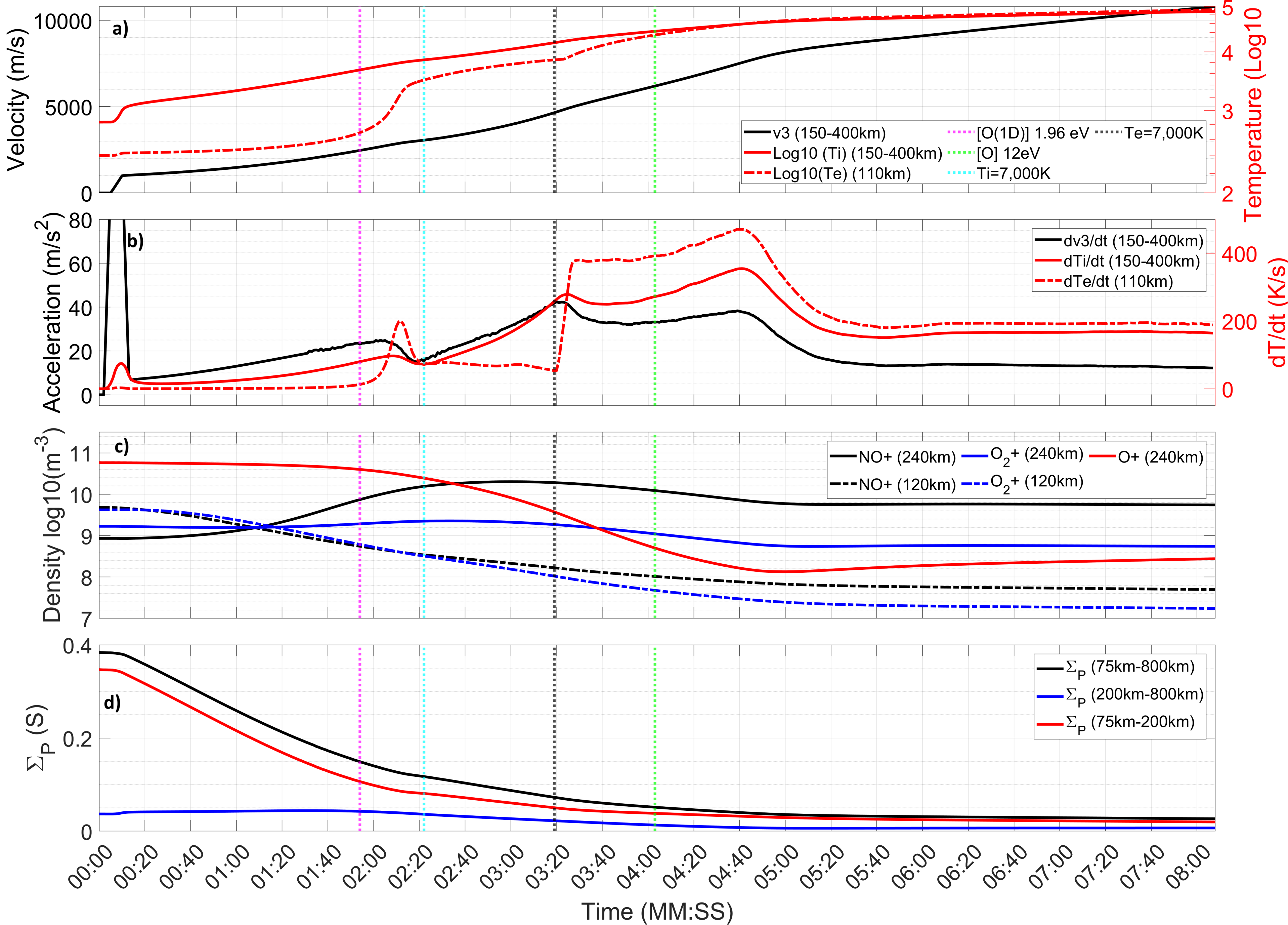


Figure 4.

Plasma parameter field aligned vertical profiles. LON=90.6

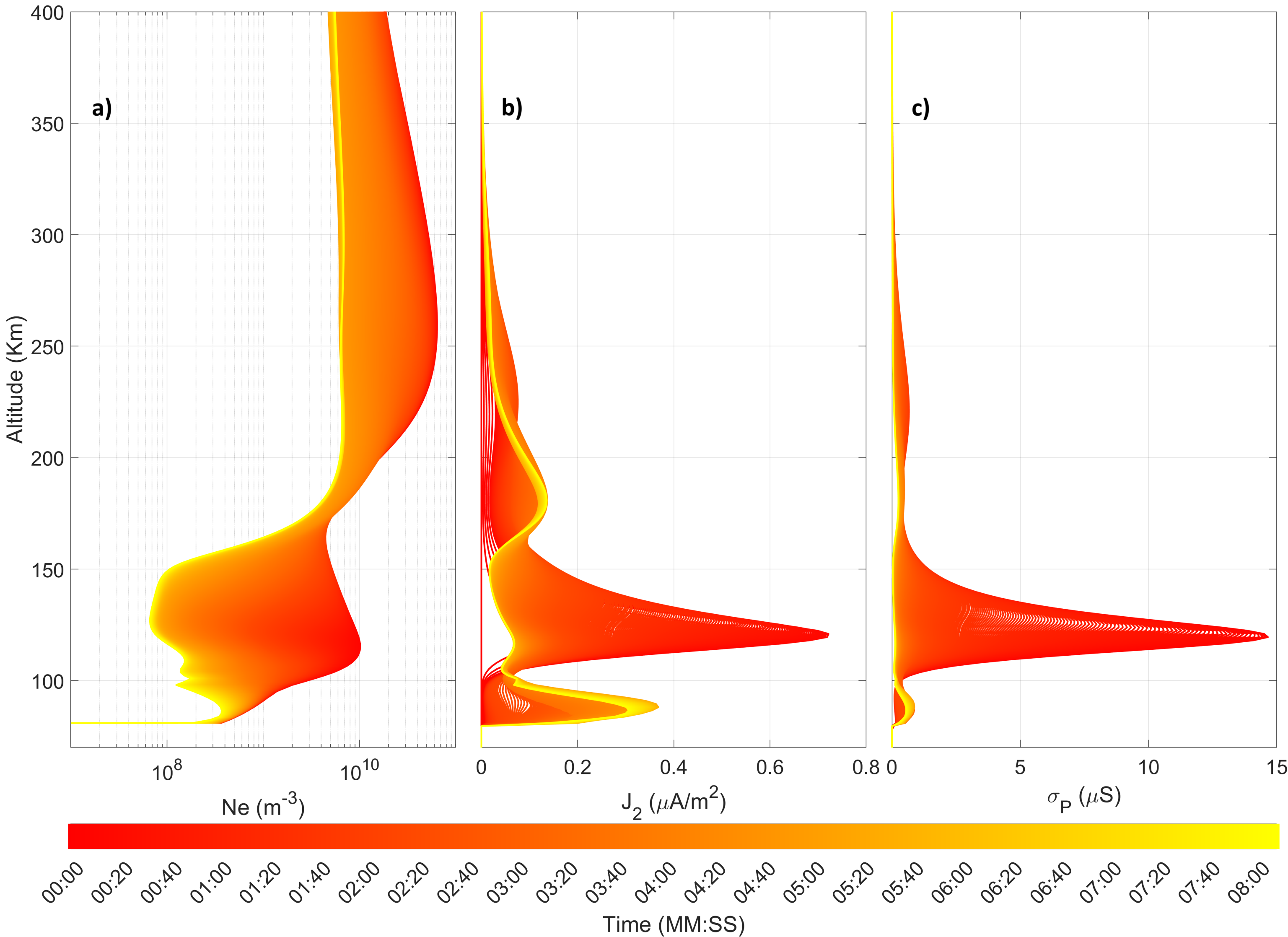
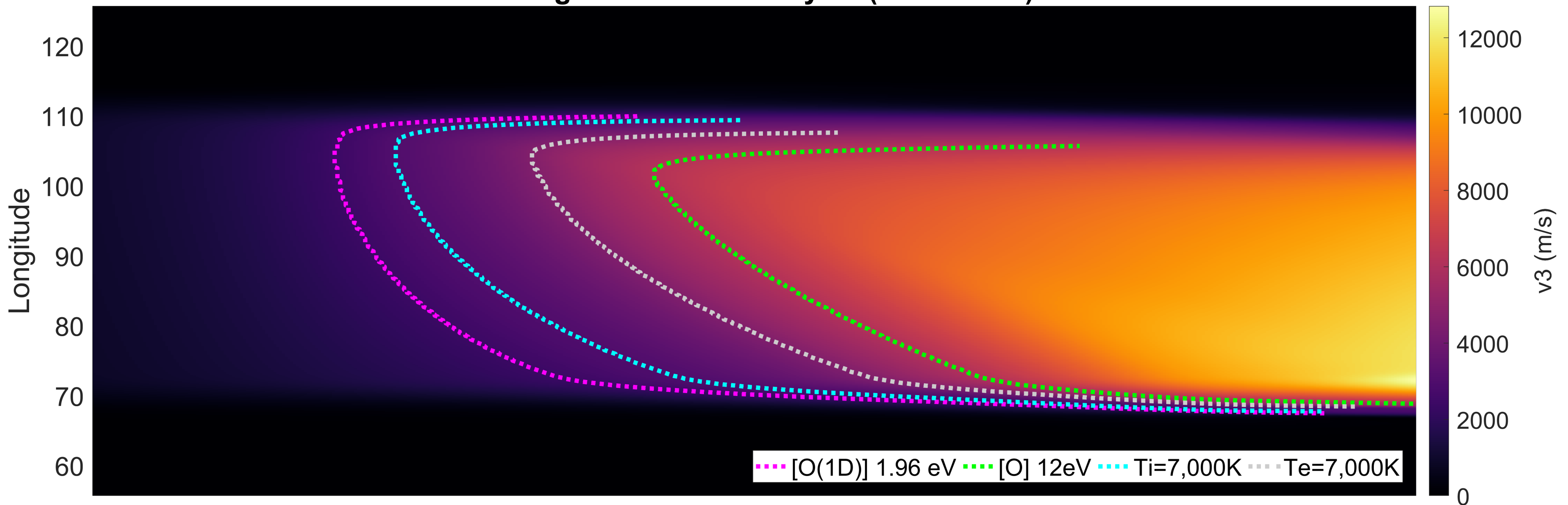


Figure 5.

Average channel velocity v_3 (150-400km)



Average channel acceleration dv_3/dt (150-400km)

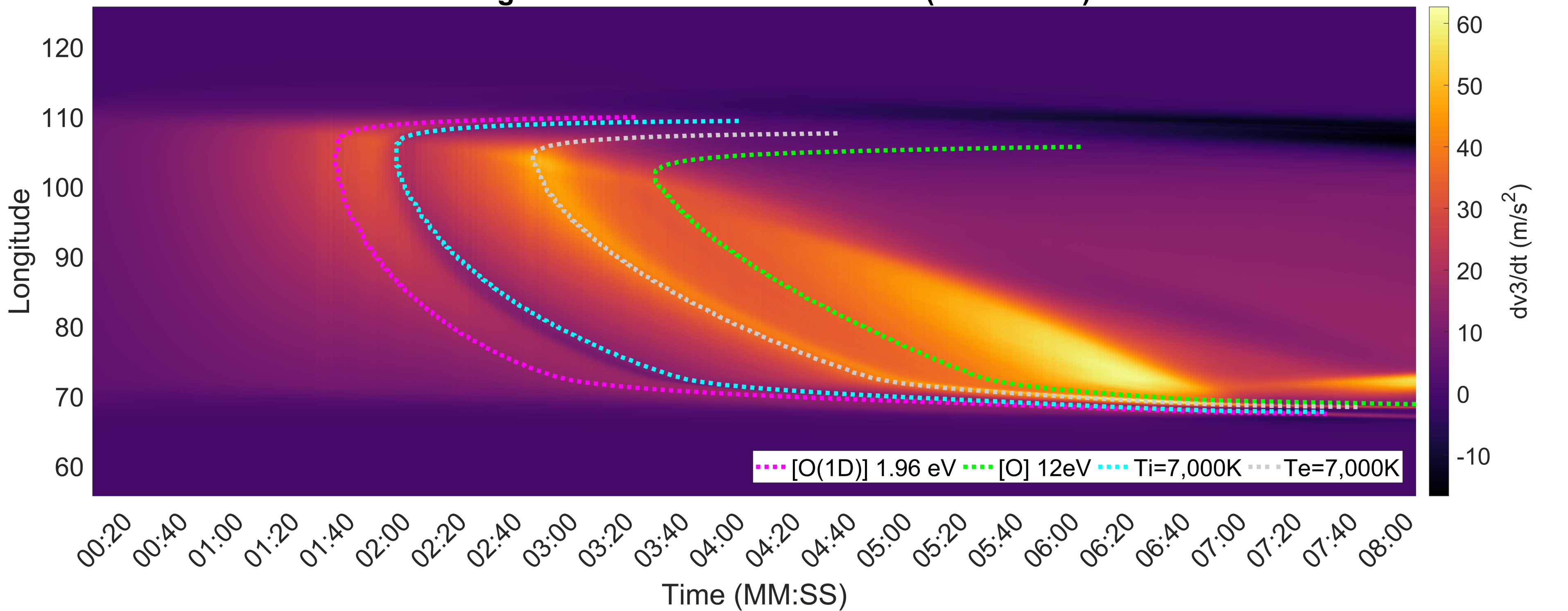
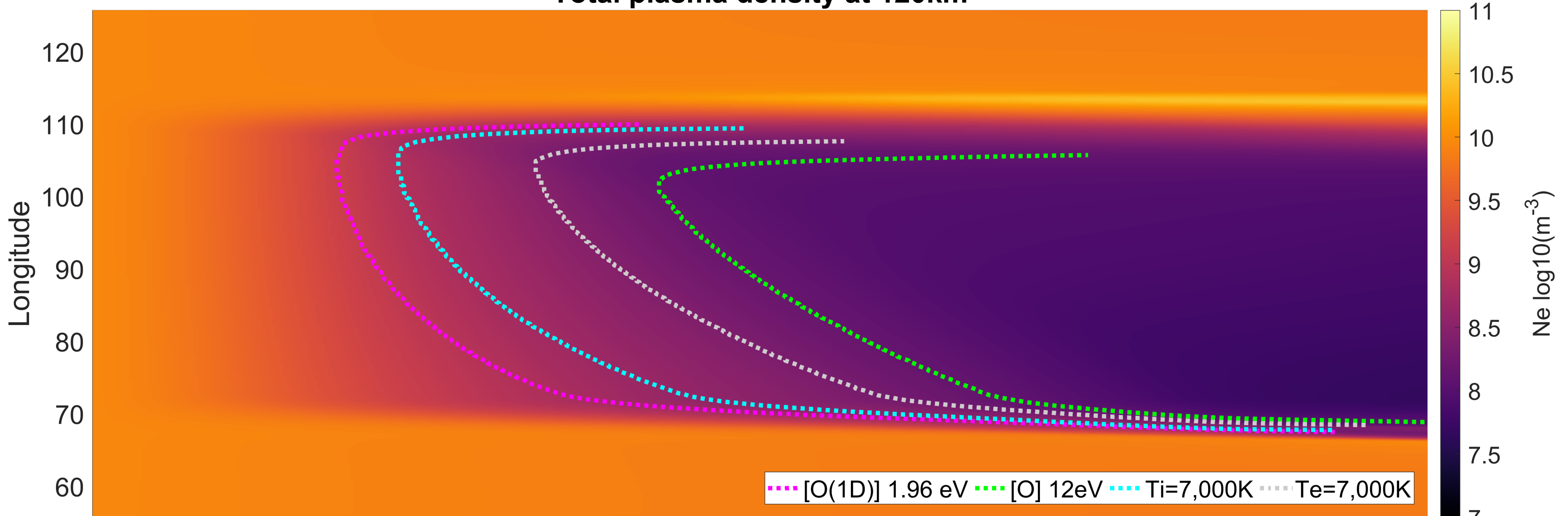


Figure 6.

Total plasma density at 120km



Total plasma density at 240km

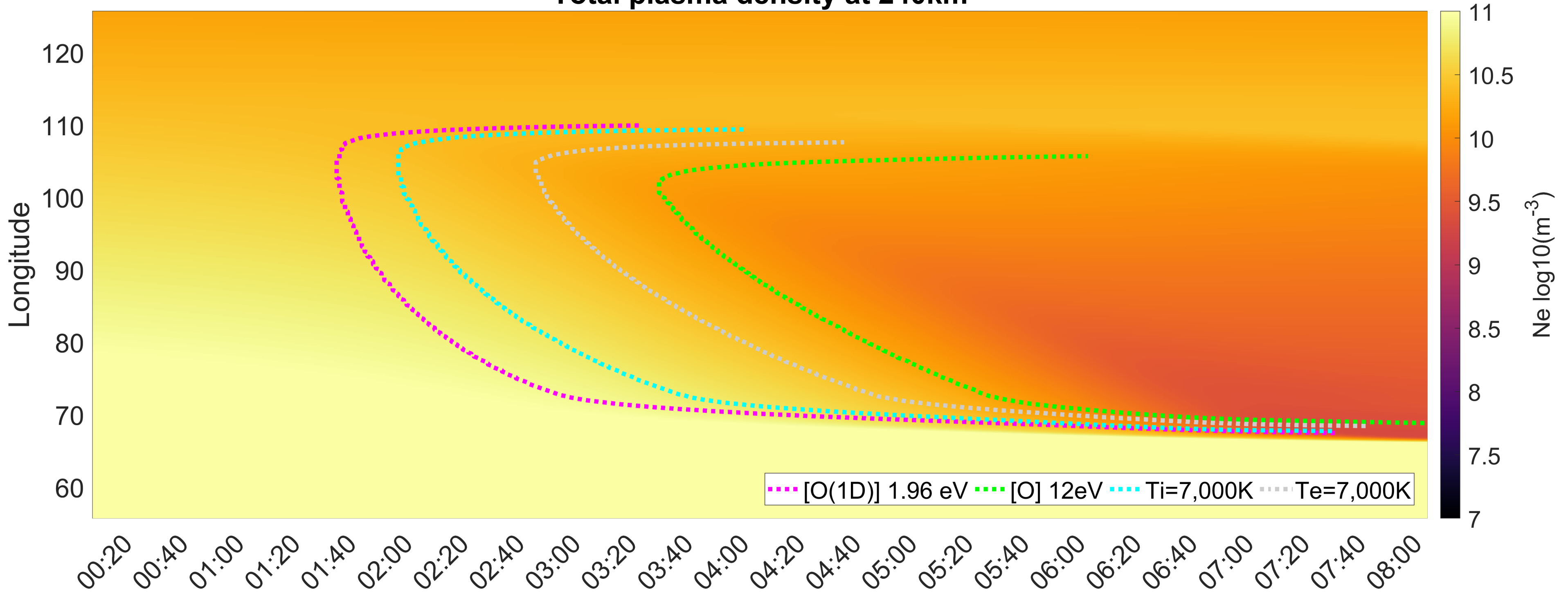


Figure 7.

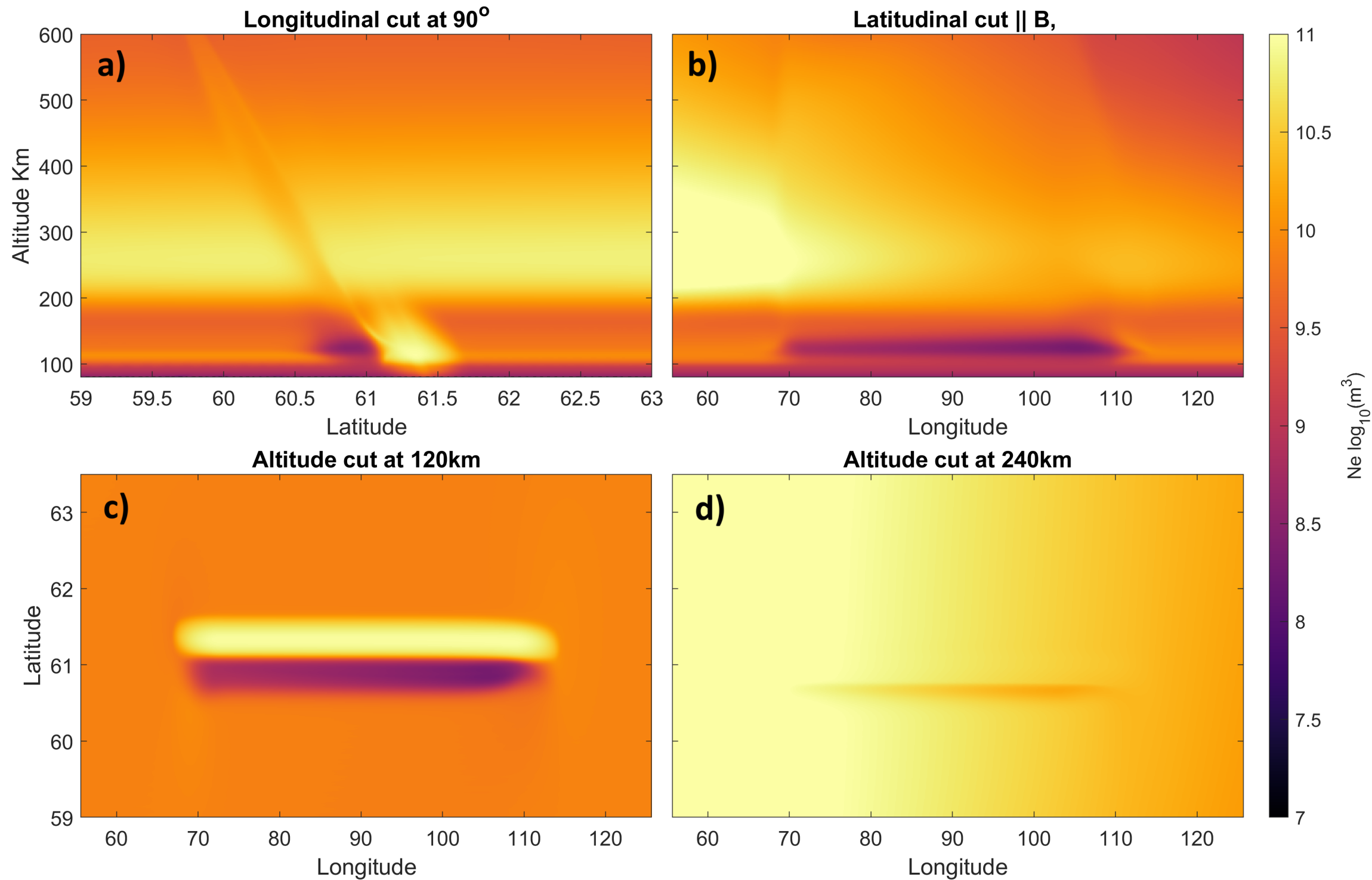


Figure 8.

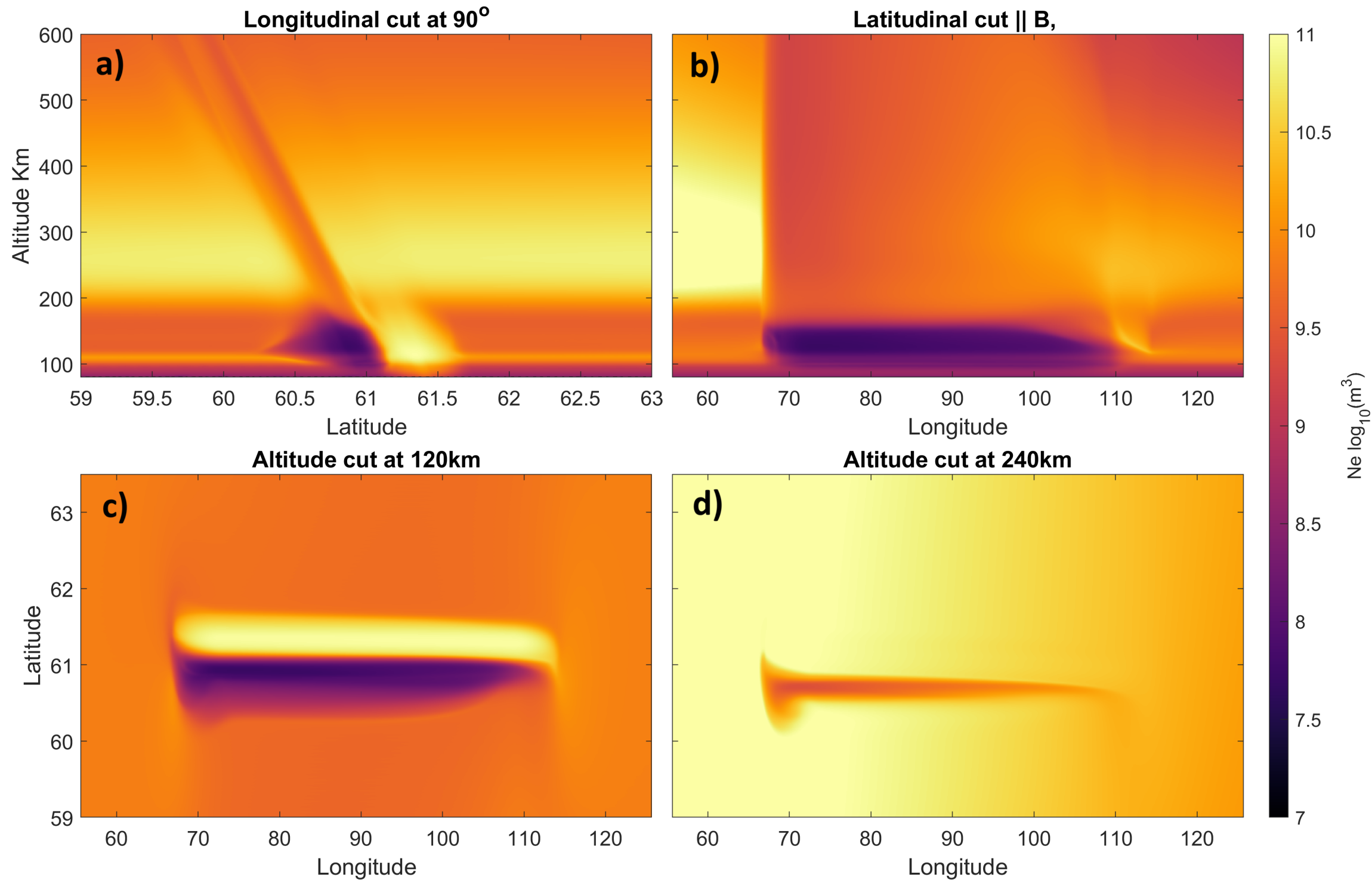


Figure 9.

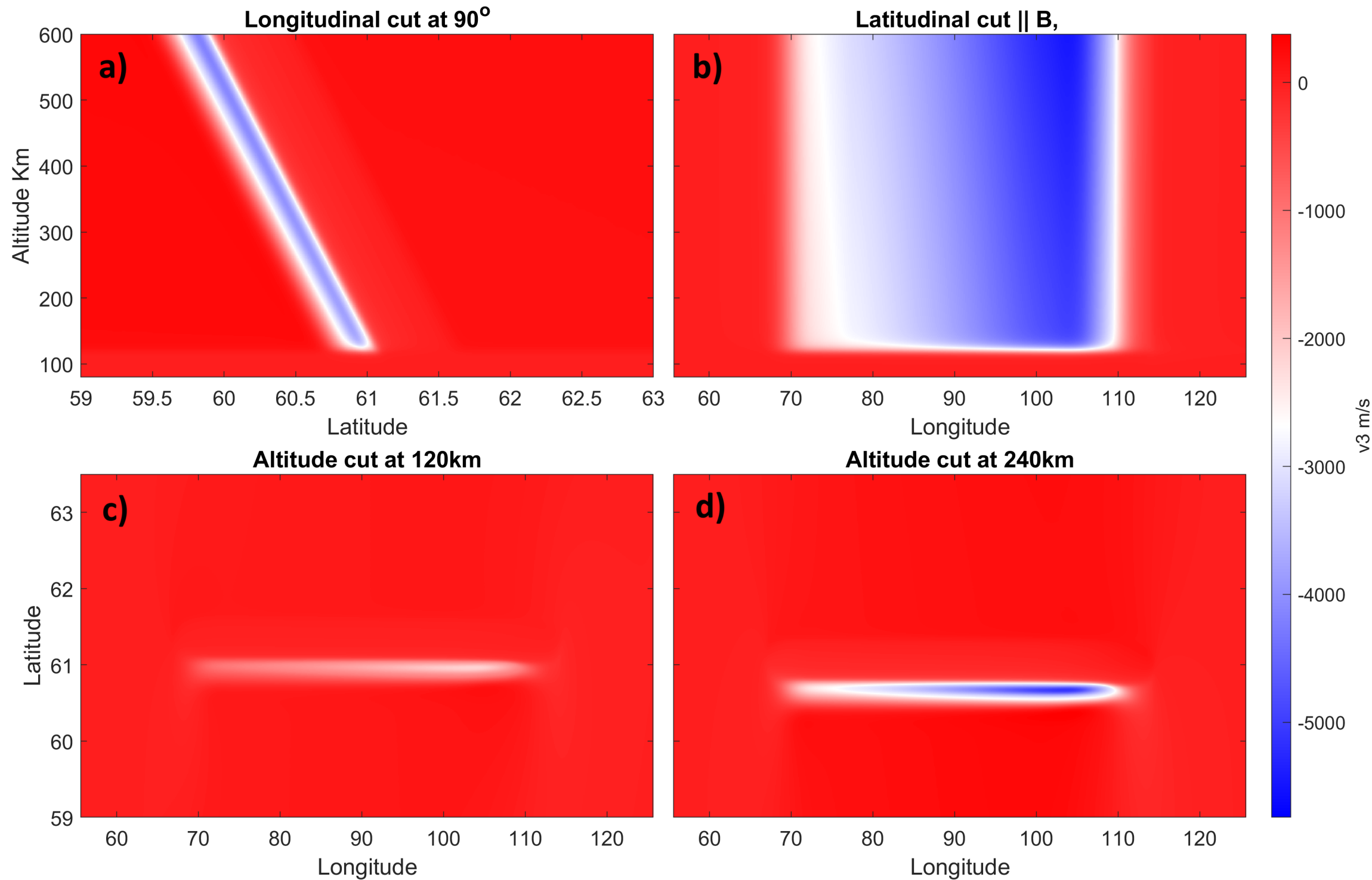


Figure 10.

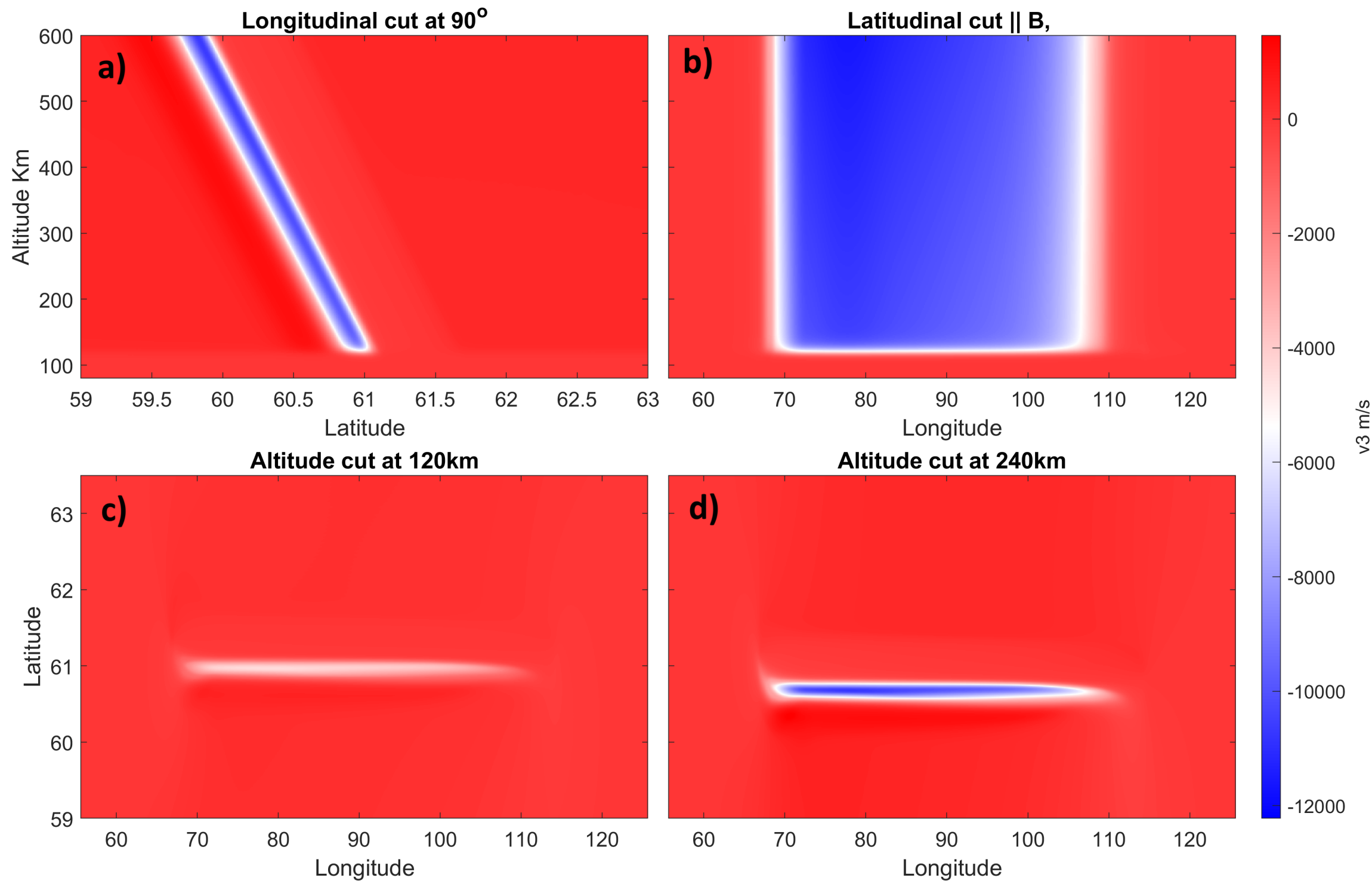


Figure 11.

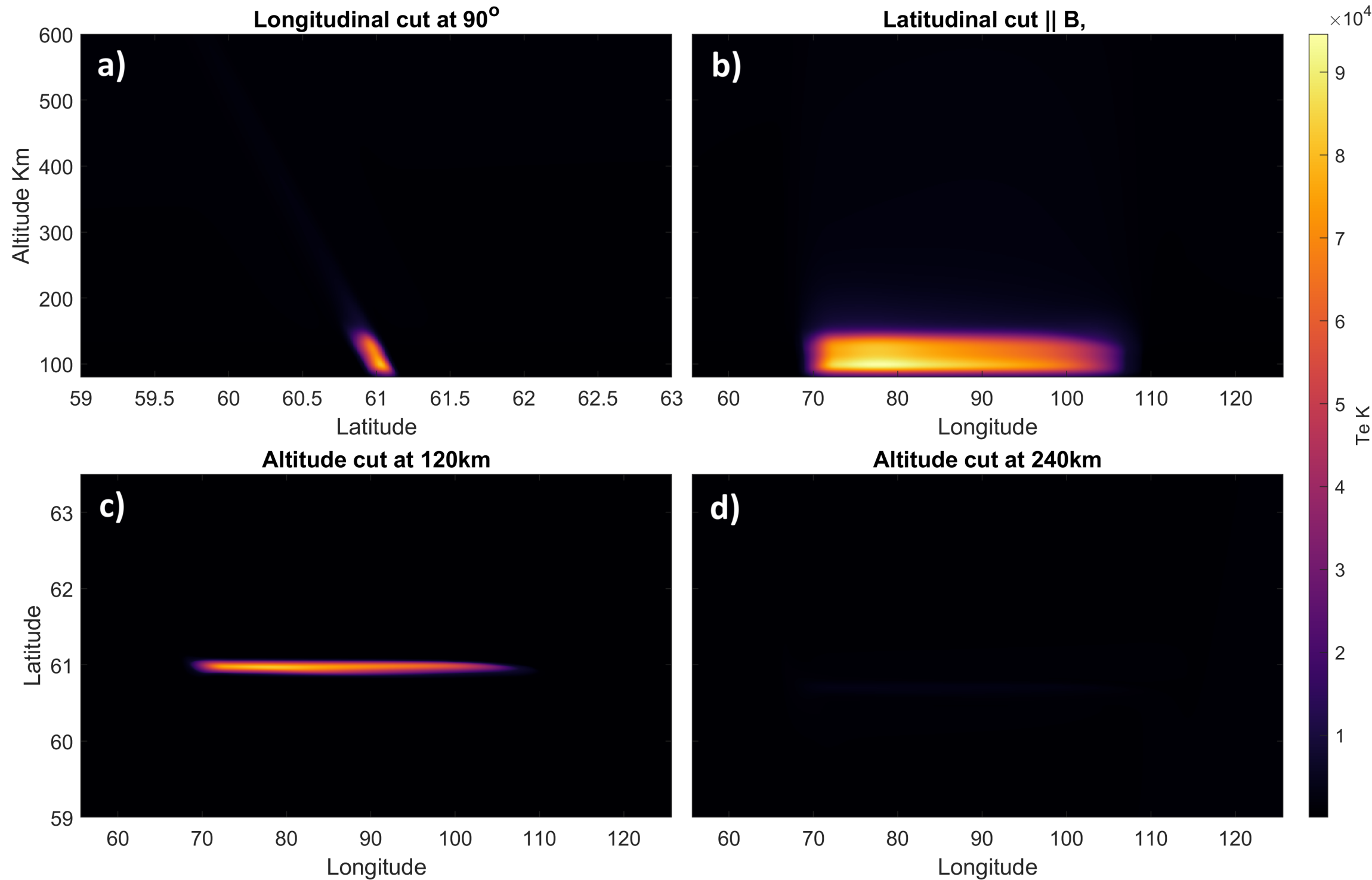
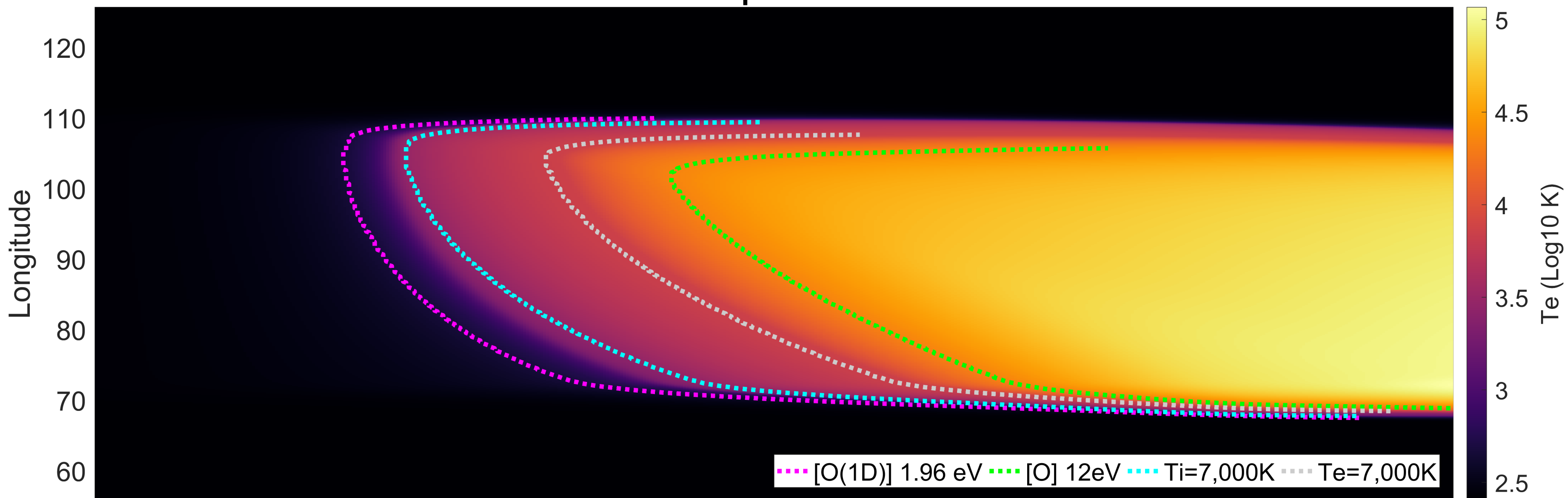


Figure 12.

Electron Temperature at 110km



J_2 at 100km

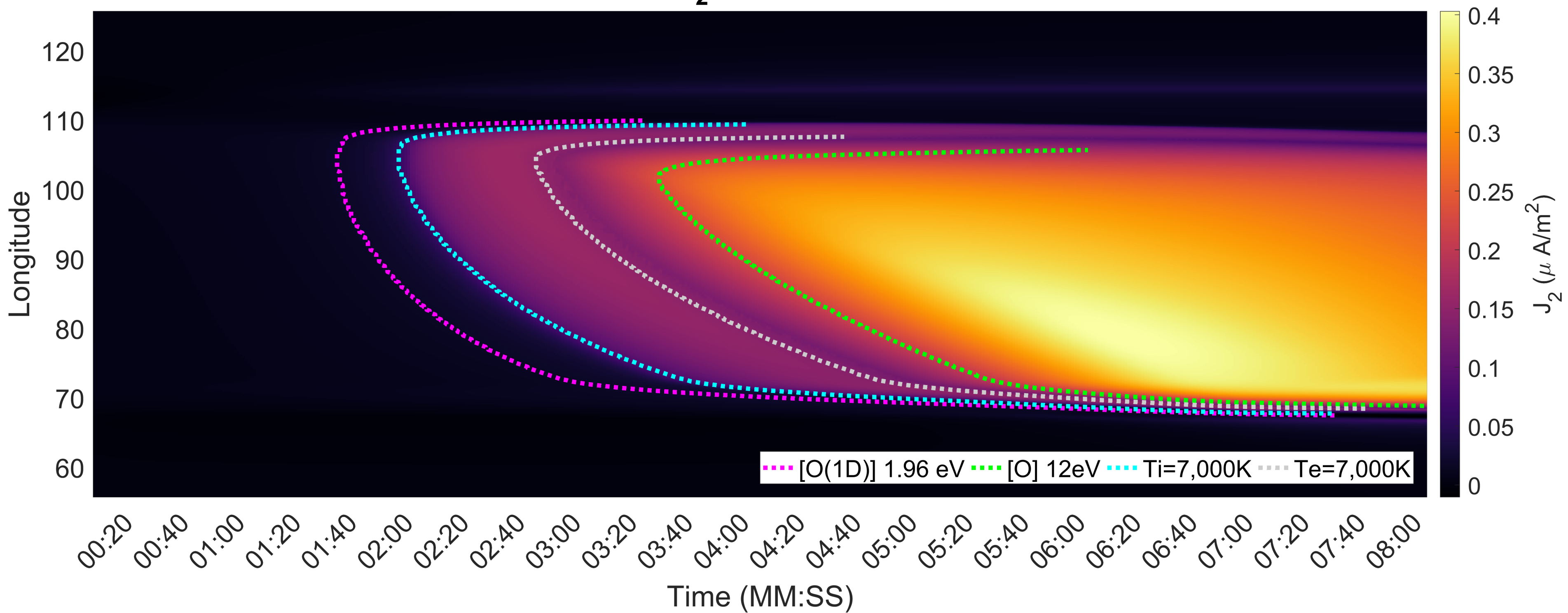


Figure 13.

Field-aligned plasma parameters RTI. LON=90.7

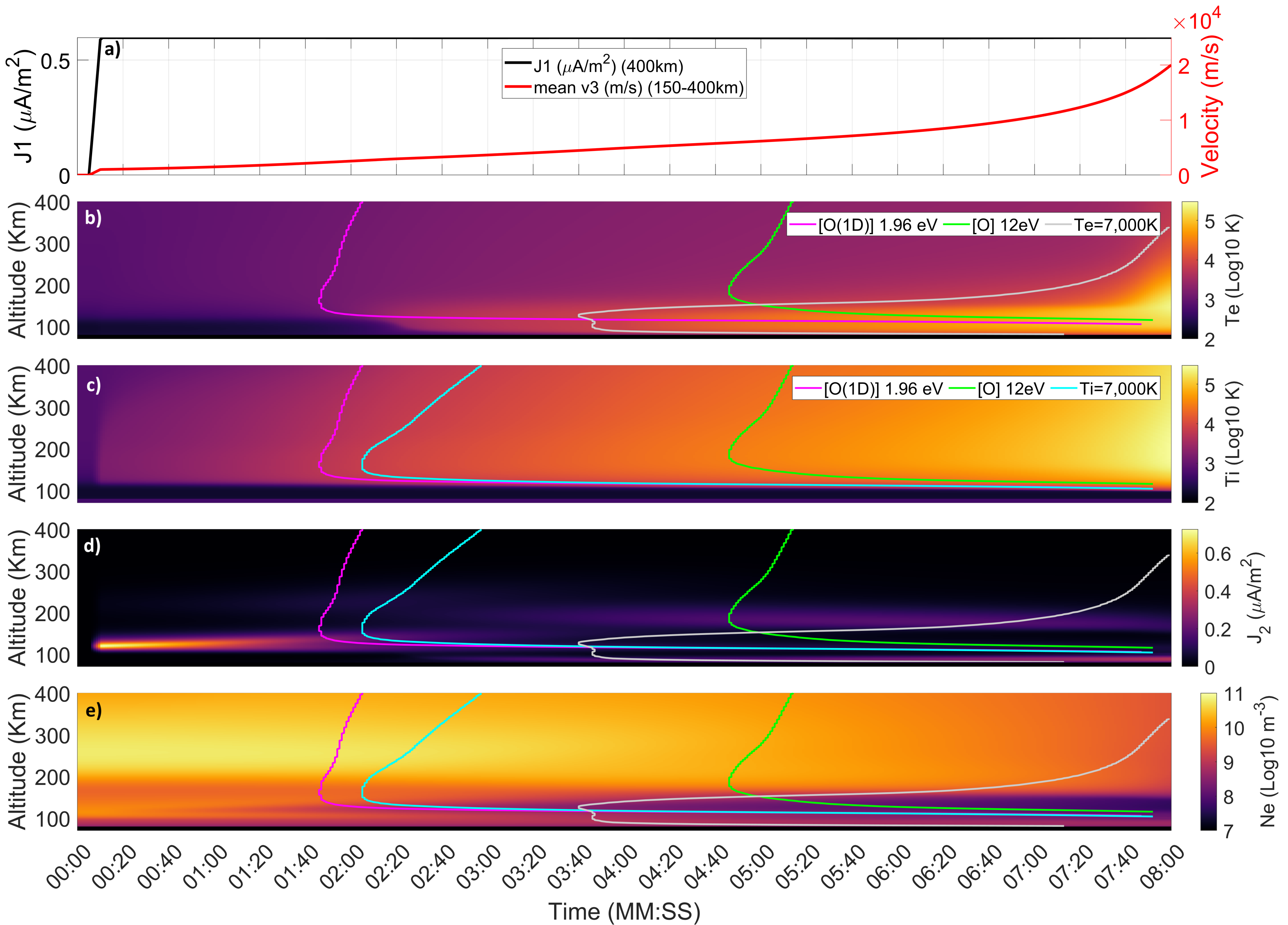


Figure 14.

Plasma parameters. LON=90.7

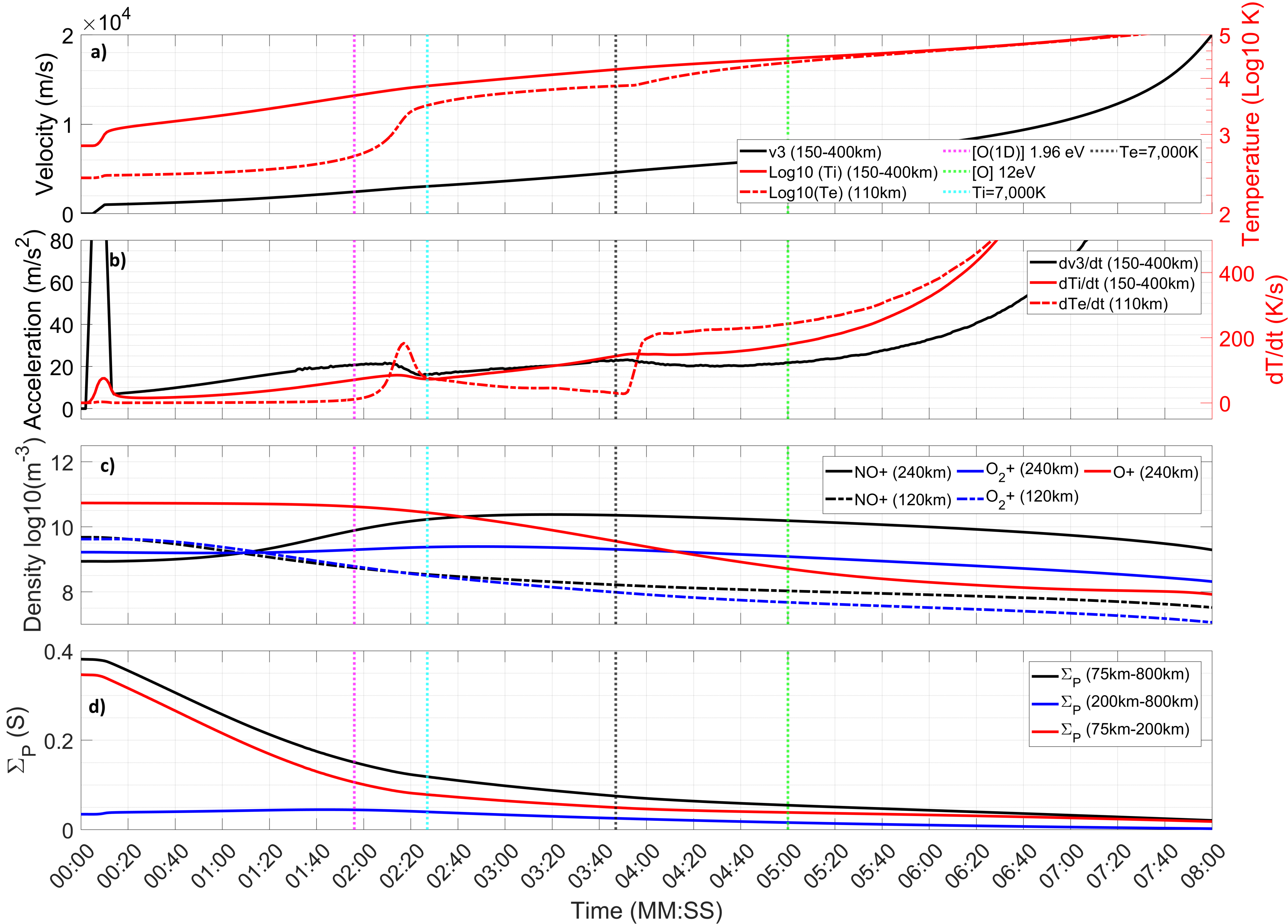


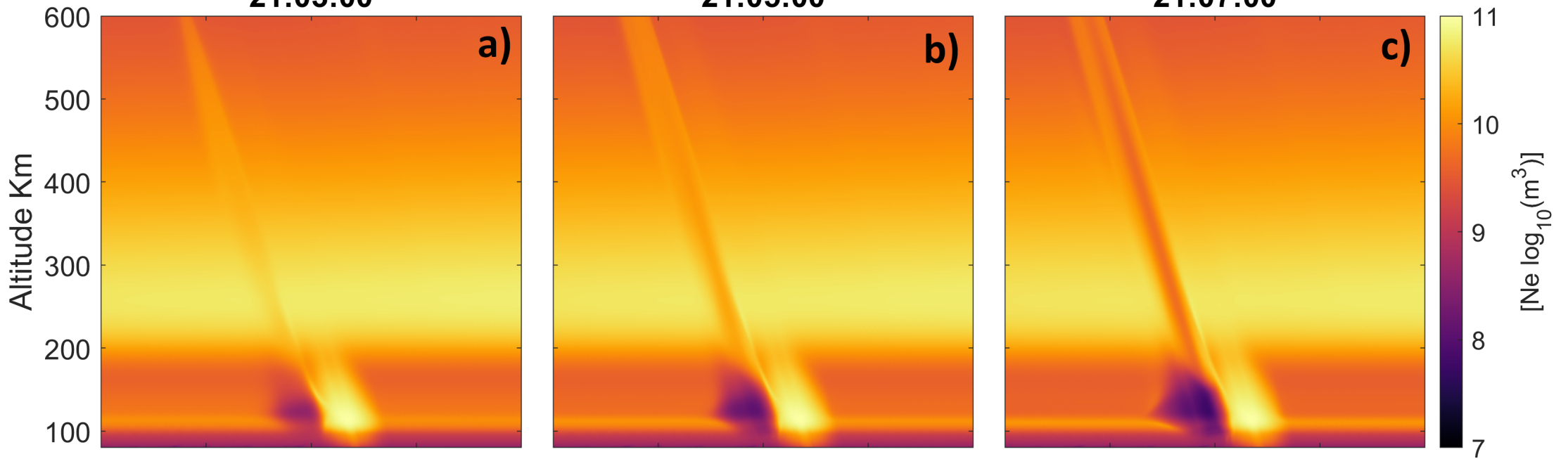
Figure 15.

2D plot of Ne 26-Mar-2008

21:03:00

21:05:00

21:07:00



2D plot of v3

